

CARBIDE COMPOSITION CHANGES IN
POWER PLANT STEELS
AS A METHOD OF
REMANENT CREEP LIFE PREDICTION

By
Rachel Clare Thomson
Newnham College, Cambridge

Department of Materials Science and Metallurgy
Pembroke Street
Cambridge
CB2 3QZ

*A dissertation submitted for the
degree of Doctor of Philosophy*

September 1992

Declare the past, diagnose the present, foretell the future.

Epidemics, Book I, Section 11

Hippocrates of Cos, *ca* 460–*ca* 357 BC

PREFACE

This dissertation is submitted for the degree of Doctor of Philosophy at the University of Cambridge. It contains an account of research carried out between October 1989 and September 1992 in the Department of Materials Science and Metallurgy, Cambridge, under the supervision of Dr. H.K.D.H. Bhadeshia. Unless appropriately referenced, the work is original and is not the result of collaboration. No part of this dissertation has been, or is currently being, submitted for any degree or diploma at this, or any other, university. This dissertation contains less than 60,000 words.

Rachel Thomson
September 1992

ACKNOWLEDGEMENTS

I wish to thank Professor C. Humphreys for the provision of laboratory facilities in the Department of Materials Science and Metallurgy at the University of Cambridge. I am indebted to Dr H.K.D.H. Bhadeshia for his encouragement and enthusiasm during the course of this work.

I would like to thank both National Power and the Science and Engineering Research Council for providing financial support for this project, and especially Dr D. Gooch of the National Power Technology and Environment Centre (NPTEC), Leatherhead, for the helpful discussions and interest he has shown in this work. I must also thank Mrs P. Dolbear at NPTEC for her assistance with X-ray diffraction studies.

I am also grateful to the staff at the National Physical Laboratory, Teddington, particularly Mr H. Davies and Dr A. Dinsdale, for the provision of MTDATA, a program for the calculation of chemical equilibria in multicomponent systems, and their advice on its use.

Thanks are also extended to the technical staff of the department who have contributed to this project; in particular, Mr D. Nicol for valuable advice on electron microscopy and carbon replica preparation, Mr J. Leader for his general ability to get equipment working, the photographic department – Mr B. Barber and Mrs C. Best for their generous help, and Mr G. Morgan and his staff in the workshop for making some of my specimens.

I must also thank my friends and colleagues in the department, especially Dr R. Reed (now of Imperial College) for his early help with transmission electron microscopy, Dr C. Boothroyd for his help with scanning transmission electron microscopy, G. Rees, M. Gregg and J. Race. My thanks also go to the other members of the Phase Transformations group, with whom it has been very enjoyable to work. I am also grateful to I. Redfern for his assistance with computing matters. Helpful discussions with Drs S. Babu, H. Harada, M. Miller, J. Whiteman and Professors C. Atkinson and G. Olson are acknowledged with pleasure.

Finally, I wish to thank my family for their unfailing support and encouragement.

ABSTRACT

The prediction of the remanent creep [†] life of a component requires a knowledge of both the service stresses and temperatures. Temperature data are subject to considerable scatter due to spatial variations around the components, and irregular fluctuations with time as a result of changes in the mode of plant operation. It has been shown that a change of about 10°C can lead to a corresponding change in the remanent life estimate by a factor of two. It is therefore desirable to be able to estimate the average thermal history of each component in order to accurately assess its remaining creep life, thereby avoiding premature replacement whilst maintaining safety standards. In this work, changes in the steel microstructure are related to the thermal history, thereby enabling the microstructure to be used as an *in situ* **time–temperature recorder**.

When many of the conventional power plant steels entered service, their microstructures contained relatively fine particles of cementite whose substitutional solute concentration was initially similar to the solute content of the steel as a whole. These carbides were far from their equilibrium chemical composition, size and shape. During service at high temperatures the cementite tends to approach its equilibrium composition with respect to the substitutional elements, which can, in principle, be used to estimate the thermal history of the component. The purpose of this work is to determine the fundamental factors controlling the rate at which carbide compositions change, so that the extrapolation of experimental data can be made with greater confidence.

Experimental studies have been made using energy–dispersive X–ray analysis in a transmission electron microscope of the kinetics of cementite enrichment in steels which have pearlitic, bainitic or martensitic microstructures. Simultaneous measurement of particle size and composition over a wide range of tempering times at various temperatures have established the fact that smaller particles enrich more quickly than larger ones.

Power plant components can be very large, with the microstructure varying considerably within a given component. Since the formation of allotriomorphic ferrite causes an increase in the carbon concentration of the residual austenite, which subsequently transforms to bainite, the distribution and scale of cementite precipitation is also expected to vary significantly with the volume fraction of bainite. Theory indicates that the rate at which the cementite particles change composition will also differ as a consequence. For example, the cementite in regions

[†] Creep deformation is the time–dependent plastic extension which a material undergoes when subject to a load at elevated temperature for a long period of time.

containing less bainite is expected to enrich at a lower rate compared with those particles in regions with a large amount of bainite. The effect of typical variations in the microstructure on cementite enrichment kinetics is studied for different volume fractions of allotriomorphic ferrite and bainite in $2\frac{1}{4}\text{Cr1Mo}$ steel.

A theoretical model has been developed of the diffusion of substitutional solute elements to cementite particles in microstructures typical of power plant steels, subject to the thermodynamic constraints which determine the equilibrium composition of the two phases. The theoretical predictions have been compared with experimental observations in $\frac{1}{2}\text{Cr}\frac{1}{2}\text{Mo}\frac{1}{4}\text{V}$ and $2\frac{1}{4}\text{Cr1Mo}$ steels. The theoretical modelling of the diffusion fields around enriching particles has highlighted the need for the compositions of the substitutional solute elements at the ferrite/cementite interface to be known accurately. The composition–distance profiles of alloying elements through a particle have therefore been studied using atom probe field ion microscopy and scanning transmission electron microscopy to establish whether in fact local equilibrium exists at the carbide/matrix interface.

Extension of the model to treat enrichment and coarsening simultaneously has been considered. In reality, both these processes contribute significantly in the approach towards equilibrium, especially at the later stages of service. It has been shown that the driving forces for the processes of enrichment and coarsening in fact compete against one another and that the coarsening process is defeated by enrichment process until the particles are close to their equilibrium composition.

At long service times, all of the common power plant steels are expected to precipitate more stable alloy carbides, at the expense of cementite. Alloy carbide precipitation has been investigated in a 12Cr1Mo1V steel in which the enrichment kinetics are much faster than in a low alloy steel. However, it has been found that the equilibrium alloy carbide precipitates during the commercial stress–relief heat treatment and does not change in composition during further tempering. This is an important result; indications are that once the cementite transforms to alloy carbides, any changes in their composition are not large enough for this method to be used as a quantitative estimation of remanent life. Low alloy steels, however, contain cementite for a considerable fraction of their useful service life.

CONTENTS

Preface	ii
Acknowledgements	iii
Abstract	iv
Contents	vi
Nomenclature and Abbreviations	viii
Chapter 1: Introduction to Remanent Life Prediction	1
1.1 Introduction	2
1.2 Methods of remanent life prediction	9
1.3 Possible future indicators of thermal history	20
1.4 Conclusions	20
Chapter 2: Physical Metallurgy Of Alloyed Steels	22
2.1 Introduction	23
2.2 Bainite	26
2.3 Martensite	30
2.4 Summary of transformation mechanisms	36
2.5 Carbide precipitation	37
2.6 Interphase precipitation	41
Chapter 3: Theoretical Studies – An Introduction	43
3.1 Introduction	44
3.2 Partitioning in pearlitic and bainitic cementite	44
3.3 Equilibrium compositions of cementite and ferrite	46
3.4 Diffusion coefficients	48
3.5 One dimensional modelling	49
3.6 Consideration of the effect of particle size	57
Chapter 4: Experimental Procedure	60
4.1 Introduction	61
4.2 Materials	62
4.3 Heat treatments	62
4.4 Hardness measurements	63
4.5 Optical microscopy	63
4.6 Transmission electron microscopy	64
4.7 Energy dispersive X–ray analysis	67
4.8 Particle size measurements	70
4.9 Bulk extraction of carbides and X–ray diffraction	71
Chapter 5: $2\frac{1}{4}$Cr1Mo Steel	73
5.1 Introduction	74
5.2 Materials	75
5.3 Initial heat treatments	76
5.4 Tempering heat treatments	92
5.5 Results and discussion from bainitic microstructures	94
5.6 Results and discussion from mixed microstructures	131
5.7 Comparison of experimental results and theoretical predictions	141
5.8 Conclusions	142

Chapter 6: $\frac{1}{2}\text{Cr}\frac{1}{2}\text{Mo}\frac{1}{4}\text{V}$ Steel	146
6.1 Introduction	147
6.2 Materials and heat treatment	147
6.3 Experimental results	148
6.4 Modelling of the diffusion process	152
6.5 Conclusions	160
Chapter 7: 12Cr1MoV Steel	161
7.1 Introduction	162
7.2 Materials and heat treatment	162
7.3 Results	163
7.4 Discussion	177
7.5 Conclusions	177
Chapter 8: Atom Probe and STEM Investigations	179
8.1 Introduction	180
8.2 Atom probe field ion microscopy	182
8.3 Scanning transmission electron microscope studies	190
8.4 Conclusions	192
Chapter 9: Further Theoretical Studies	193
9.1 Introduction	194
9.2 Experimental studies of particle coarsening	194
9.3 Particle size and solubility	196
9.4 Approximations	199
9.5 Application to simultaneous coarsening and enrichment of cementite	200
9.6 Conclusions	202
Chapter 10: Conclusions and Suggestions for Future Work	204
APPENDIX I	207
APPENDIX II	209
APPENDIX III	214
REFERENCES	219

NOMENCLATURE AND ABBREVIATIONS

a	Lattice parameter
at. %	Concentrations in atomic percent
A	Constant
A	Number of cavitating grain boundaries
A_{e_1}	Temperature of the eutectoid reaction
A_{e_3}	Temperature separating the $\alpha + \gamma$ and γ phase fields for a specific alloy
b.c.c.	Body-centred cubic
B	Constant
B_s	Bainite start temperature
c	Speed of light in vacuo
c	Thickness of a plate
c'	Dimensionless concentration in the finite difference method
$c^{\alpha\theta}$	Concentration in ferrite in equilibrium with cementite
$c^{\theta\alpha}$	Concentration in cementite in equilibrium with ferrite
c_{∞}^{α}	Equilibrium concentration in ferrite
c_{∞}^{θ}	Equilibrium concentration in cementite
c_r^{α}	Equilibrium concentration in ferrite at the ferrite/cementite interface
c_r^{θ}	Equilibrium concentration in cementite at the ferrite/cementite interface
\bar{c}	Average concentration in the alloy
C	Constant
C_A	Weight fraction of element A
d	Interatomic spacing along a specific crystallographic orientation
D	Diffusion coefficient
D_0	Pre-exponential factor for the diffusion coefficient
D_{α}	Diffusivity in ferrite
D_{θ}	Diffusivity in cementite
e	Electronic charge
eV	Electron volt
E	Strain energy
EDX	Energy-dispersive X-ray analysis
f	Volume fraction of martensite
f.c.c.	Face-centered cubic
g	Chemical potential
g_0	Chemical potential of pure substance
G_m	Molar Gibbs free energy
h	Planck's constant
HP	High pressure
HV	Vickers Hardness units
I	Integrated intensity per unit length of diffraction line
I_A	Characteristic intensity of element A
ILS	Invariant line strain
ISO	International Standards Organisation
IP	Intermediate pressure
IPS	Invariant plane strain
k	Boltzmann constant
k_{AB}	Experimental constant
k_z	Partition coefficient with respect to element z
L	Camera length
LP	Low pressure

m	Electronic mass
M_s	Martensite start temperature
MLI	Mean Linear Intercept
MTDATA	Metallurgical and Thermodynamic Data Service
n	Number of atoms
n_α	Number of slices of ferrite
n_θ	Number of slices of cementite
N	$\sqrt{h^2 + k^2 + l^2}$ where h , k and l are plane indices
N_A	Avagadros number
NDT	Non-destructive testing
NP-LE	Negligible partitioning local equilibrium
NPL	National Physical Laboratory
O	Surface area
P-LE	Partitioning local equilibrium
q	Half thickness
Q	Activation free energy per mole for diffusion
r	Grid parameter in the finite difference method
r	Radius of a spherical particle
r	Length of a plate
R	Universal gas constant
R	Distance between transmitted and diffracted electron beams
s	Shear component of a shape deformation strain
ss	Supersaturated
S_v	Grain surface area per unit volume
STEM	Scanning Transmission Electron Microscopy
t'	Dimensionless time in the finite difference method
t	Time
t_c	Time to reach a specific concentration
t_i	Time
t_{if}	Failure time
T	Temperature
T_i	Temperature
T_o	Temperature at which austenite and ferrite of the same composition have the same free energy
T'_o	As T_o but accounting for the stored energy of ferrite
TEM	Transmission Electron Microscopy
TTT	Time-Temperature-Transformation
us	Unsaturated
V	Volts
V_b	Volume fraction of bainite
V_m	Molar volume
V^α	Volume fraction of ferrite
V^θ	Volume fraction of cementite
W_s	Widmanstätten ferrite reaction start temperature
wt.%	Concentrations in weight percent
\bar{x}	Mean concentration in bulk alloy
x_z	Mole fraction of element z
x_s	Thickness of slice in finite difference method
x_{T_o}	Carbon concentration in austenite at end of bainite reaction
x'	Dimensionless distance in the finite difference method
x_α	Concentration in ferrite

x_α	Half-thickness of ferrite in diffusion couple
x_θ	Thickness of cementite in diffusion couple
$x^{\gamma\alpha}$	Concentration (of carbon) in austenite in equilibrium with ferrite
$x^{\alpha\gamma}$	Concentration (of carbon) in ferrite in equilibrium with austenite
y_z	Concentration of element z
α	Ferrite
α_1	One-dimensional parabolic thickening rate constant
α'	Martensite
α_{1b}	Lower bainite
α_{ub}	Upper bainite
α_w	Widmanstätten ferrite
γ	Austenite
γ	Interfacial free energy per unit area
γ_{en}	Enriched austenite
Γ	Activity coefficient
δ	Dilational component of a shape deformation strain
ΔT	Metal-to-steam temperature differential
ϵ	Epsilon carbide
ζ	Volume fraction of allotriomorphic ferrite
θ	Bragg angle
θ	Cementite
λ	Wavelength
λ	Absolute activity
λ_o	Absolute activity of pure substance
μ	Shear modulus
σ_i	Stress
σ_{ref}	Reference stress
ϕ	Equilibrium volume fraction of ferrite

CHAPTER 1

INTRODUCTION TO REMANENT LIFE PREDICTION

This chapter provides a general introduction to my research and contains a review of remanent life prediction procedures.

CHAPTER 1

INTRODUCTION TO REMANENT LIFE PREDICTION

1.1 Introduction

High temperature power and process plant components are designed to codes which define a conservative useful life. Therefore, it could be supposed that the plant will give satisfactory service up to, but not much beyond the design life. However, experience has shown that many power plant can operate safely for times significantly longer than their design lives. Therefore two distinct parts of service can be defined:

- (a) the original design life, and
- (b) the safe economic life (which is outside the influence of the design codes but may be a significant fraction of the total service life).

Materials operating at high temperatures under creep conditions have a finite operating life and so consideration must be given to a 'beyond design' end-of-life criterion.

The assessment of the remanent creep life [†] in carbon and low-alloy steel components operating at elevated temperatures has, in recent years, received increased attention from power generation authorities, petrochemical companies and government inspection and certification agencies throughout the world.

In England and Wales there are at least 54,000 MW of electricity generating capacity, including 12 power stations which between them contain a total of 41 highly efficient 500 MW coal fired units. These stations have comparatively low operating costs and are therefore used for every day (base-load) generation. However, these stations were built in the 1960s and 1970s, individual units having now reached total operating times in the range 90,000–120,000 hours. It has been established that it is economically desirable and technically possible to extend the lives of these stations to periods in excess of 250,000 hours.

1.1.1 Replacement strategy

In order to implement this policy, the criteria which determine whether or not a component should be replaced need to be considered. Two possible options have been investigated:

- (a) After 150,000 hours service to replace all major components which can be shown to survive 150,000 hours, but which cannot be guaranteed to survive beyond 250,000 hours, and

[†] The remanent creep life is the service time remaining for a partially creep damaged component before creep-induced failure occurs, and relates to components operating under high temperature conditions where creep is the main mode of failure.

- (b) to replace each major component only when remanent life assessment techniques indicate that this is necessary.

The first criterion is certainly the simplest and would ease the problem of planning for refurbishment programmes since several years notification of the need for replacement could be given. This would, however, in many cases lead to the premature or completely unnecessary replacement of components which would not have been established to have an 'end-of-life' condition in terms of degradation and damage. It may also increase the periods during which the plant is not operational which would result in substantial cost penalties. The second possibility is the one adopted by the generating companies as it avoids these disadvantages and is financially beneficial. Components are not generally replaced prior to need and hence refurbishment work can be spread over the complete operating life of the units, thereby reducing the time for which the plant is not operational. However, for this strategy to be implemented it is clearly necessary to develop an accurate and reliable procedure for remanent creep life assessment, a procedure based on sound physical principles so that extrapolation over long periods of time can be carried out with confidence.

1.1.2 The need for life assessment

The reasons why remanent life appraisal is necessary can be summarised as follows:

- Safety: To meet safety regulations specified by legislative bodies and the utility insurers, and therefore to preserve the safety of personnel and plant integrity.
- Operation: To avoid costly, unscheduled plant shutdowns by preventing high temperature failures.
- Strategy: To plan for component replacement and to allow time for the manufacture of replacements and therefore to allow operation of high temperature plant beyond the original design life.

1.1.3 Procedure documents

In order to develop a life assessment procedure for a particular component, it is necessary to consider the operating regimes, the type of component and the materials from which it is manufactured, the potential failure mechanisms and the available failure statistics, and also the difficulties in repairing the component and the cost of any shutdowns. Formal procedure documents have been or are being written to assess the safe and economic life of each component and the need for replacement. The procedures are based on a system of regular monitoring of operating parameters, systematic inspection, the procurement of samples for post-service testing and the calculation of remaining life by using relevant materials data in an established

relationship describing the degradation and life-limiting failure mechanisms. An important aspect of these formal procedure documents is that they link the ‘science’ of life prediction established within the laboratory with the ‘engineering requirements’ associated with continued operation, the need for repair, or in some cases replacement, and the requirements for non-destructive testing (NDT) inspection.

1.1.4 Power plant

In a power station heat is produced by burning coal or oil (or from a nuclear pile) within a furnace. Water is supplied to the boiler from a common feed main by feed pumps. The feedwater first passes through the economiser and into the steam drum. (The economiser is situated next to the tubes containing the exit steam from the furnace walls and so it is used to preheat the feedwater before it enters the boiler.) The water is then drawn from the steam drum into the tubes lining the furnace walls, subsequently returning to the drum as a mixture of water and steam.

Water and steam are separated within the steam drum, the water being returned to the furnace wall tubes by boiler circulating pumps. Hot gases from the combustion chamber flow across the boiler horizontally to heat the superheaters, reheaters and economiser elements, before flowing to the gas airheater (to heat the incoming air to the combustion chamber). Steam from the drum then passes through the superheater pendants to the high pressure (HP) cylinder where it is directed through nozzles on to the turbine blades to rotate the turbine. Exhaust steam from the HP cylinder returns to the boiler to pass through the reheater pendants so that its temperature is restored. The reheated steam is then passed to the intermediate pressure (IP) cylinder, the exhaust from which is then passed directly into the low pressure (LP) cylinder. The HP, IP and LP cylinders are coupled together to drive the rotor of the generator. The route for water and steam circulation is illustrated schematically in Figure 1.1.

A diagram of a power station boiler and the associated steam plant (Littlebrook Power Station Guide, National Power Technical Publications) is given in Figure 1.2.

Consideration must be given to the types of component and materials likely to require accurate life prediction. In general, these will depend on plant design and operational practice. However, other criteria include the severity of the operating regime, known failure statistics, the difficulty of repair and the cost of associated outages, the cause of failure and the potential benefits to be gained by developing an accurate life predictive capability.

On the first of these criteria it is evident that boiler components offer a more pressing need than turbine components. This is because turbine components, although operating under extremely onerous conditions, nevertheless generally operate within the design parameters for

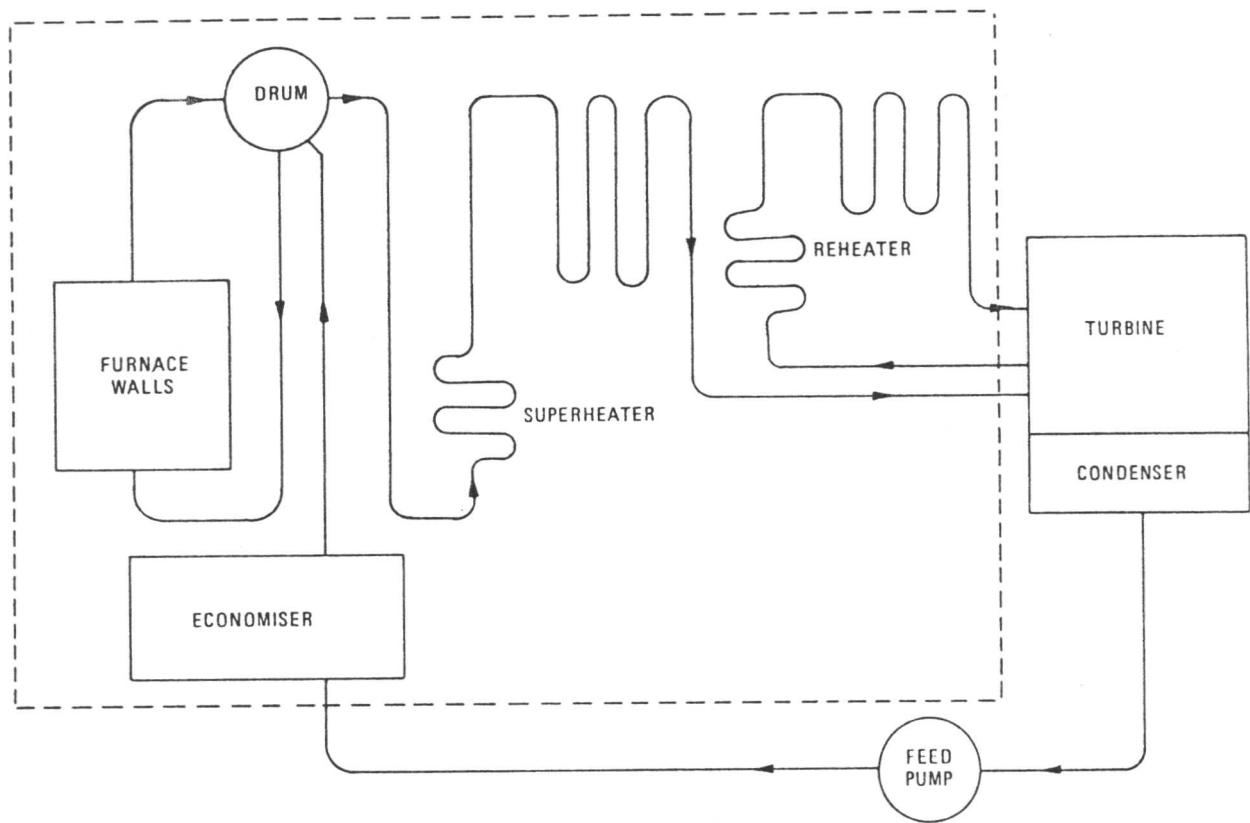


Figure 1.1: Water and steam circulation in power plant (Davison and Yeldham, 1975).

temperature, pressure and cyclic loading. Boiler components such as tubing and steam headers, however, frequently operate outside the parameters used in their design, particularly with respect to temperature and corrosive environment.

The main components which are critical are steam headers, superheater and reheater tubing in boilers, turbine valve chests, rotors and casings, main steam and reheat pipework, generator rotors and bolts used for high temperature applications. A summary of the components for which it would be possible to draw up a procedural document and their typical life limiting factor is shown in Table 1.1. The typical areas of attention for plant life extension on coal-fired power stations are illustrated in Figure 1.3.

Table 1.1: Typical life limiting factors for power station components.

Component	Typical Life Limiting Factor
<i>Boilers</i>	
Headers–superheater, reheater	Creep, thermal fatigue
Tubes–furnace wall	Fireside corrosion
Superheater, reheater	Creep, fireside corrosion
<i>Pipework</i>	
HP and RH pipework	Weld cracking, creep
Boiler and turbine valves	Weld cracking, creep, bolt failures
	Thermal fatigue
<i>Turbines and generators</i>	
Turbine valve chests	Thermal fatigue, creep, bolt failures
Turbine HP and IP casing	Thermal fatigue, creep
Turbine HP and IP rotors	Creep, fatigue
High temperature bolting	Creep, stress erosion, thermal fatigue
Generator rotors	Fatigue

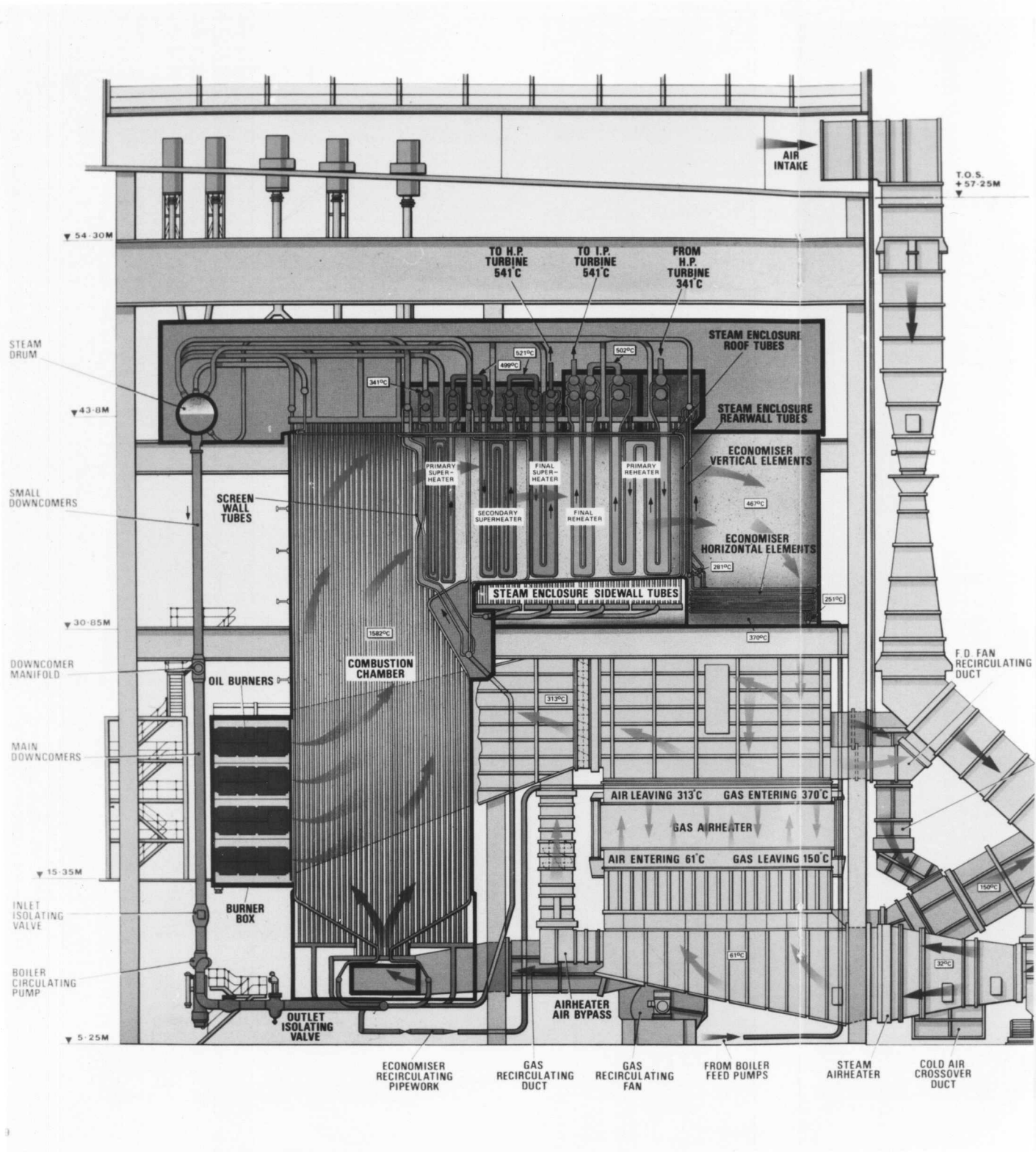


Figure 1.2

typical areas of attention for plant life extension on coal

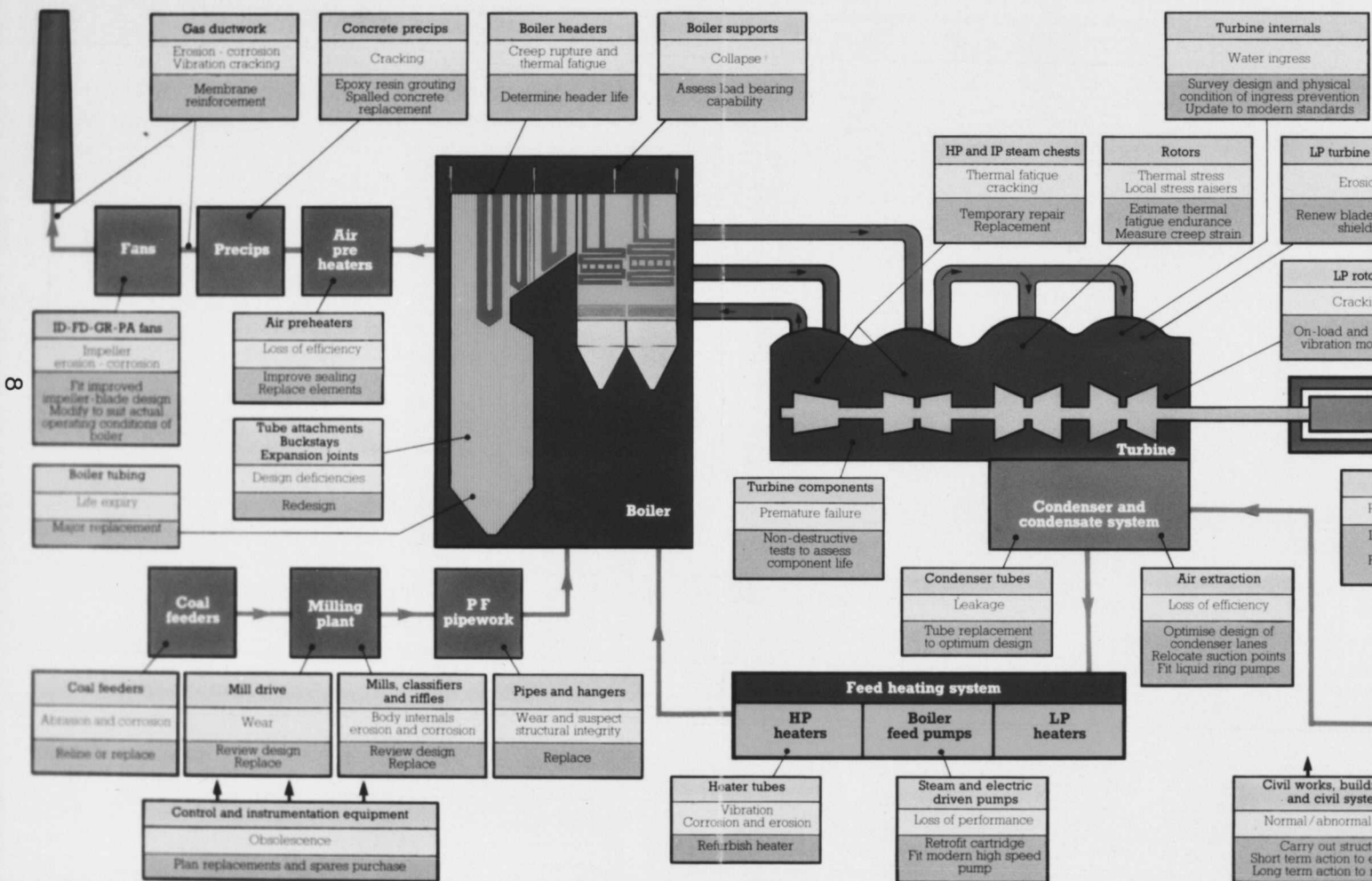


Figure 1.3

1.2 Methods of remanent life prediction

The useful life of power plant components can be limited by various damage mechanisms including creep, fatigue, wear and corrosion. This work focusses on the prediction of remanent life by estimation of the thermal history of low alloy ferritic and bainitic steels, $\frac{1}{2}\text{Cr}\frac{1}{2}\text{Mo}\frac{1}{4}\text{V}$ and $2\frac{1}{4}\text{Cr1Mo}$, and martensitic 12Cr1Mo1V steels, which ultimately fail under creep conditions. Creep strength arises from the addition of substitutional alloying elements, (Mo, Cr, V and Mn), to the base steel composition. There are two contributions to the creep strength. The first arises from solid solution strengthening, the added alloying elements making cross slip and dislocation climb more difficult (Argent *et al.*, 1970) by distorting the solvent lattice. Molybdenum, the largest of the substitutional alloying elements, is the most effective addition in solid solution strengthening. The second contribution to creep strength, which is particularly important in the later stages of service, is the ability of the alloying elements to form a stable dispersion of precipitates which hinder dislocation motion and prevent the migration of boundaries and sub-boundaries during creep. Creep resistance is attenuated as the more stable carbides coarsen, spheroidise and agglomerate (Sellars, 1974).

Creep damage itself can be said to occur by two different methods; the development of intergranular cavities leading to cracking, and secondly an acceleration of the creep rate directly related to microstructural changes such as the coarsening of initially creep resistant precipitate dispersions, changes in precipitate identity, increasing grain size or a change in the number density of dislocations. These two processes occur simultaneously and will depend on the initial heat treatment conditions, the applied stress and the temperature.

For high temperature plant investigations a wide variety of complementary techniques to estimate the remaining life of components are employed, several of which are being used under service conditions. These have been reviewed extensively (Cane and Townsend, 1984; Wilson, 1986; Cane, 1986; Cane and Williams, 1987) and the various techniques are summarised below:

- (1) Post-exposure creep testing of components.
- (2) Metallography to assess the extent of microstructural degradation, with particular emphasis on cavity nucleation and cracking.
- (3) Examination of plant operational records, e.g. temperature and pressure records taken daily, the use of standard materials data and the life fraction rule.
- (4) Estimation of the average thermal history of a component by detailed investigation of carbide composition, identity and size within the microstructure.

1.2.1 Post exposure creep testing

Creep life has most commonly been estimated using parametric relationships to extrapolate short term creep data obtained at elevated stresses and/or temperatures. Post-service evaluation techniques can clearly be classed as mostly destructive methods of assessment, to the extent that a weld repair may be needed due to the volume of material required. To obtain results in a reasonable time, the tests have to be performed under accelerated conditions by increasing stress or temperature or both. If tests are performed by accelerating the temperature at constant stress care must be taken to avoid excessive oxidation of the test piece. Tests may have to be performed under a non-oxidising environment, either in a vacuum or argon. Both creep and rupture testing have been well documented (Hart, 1976; Woodford, 1974) therefore only a brief example of the use of creep testing is presented here.

Samples were cut from a $\frac{1}{2}\text{Cr}\frac{1}{2}\text{Mo}\frac{1}{4}\text{V}$ reheater drum after 70,000 hours service and machined into specimens for creep testing (Cane and Townsend, 1984). The drum was known to be overheating and thermocouple measurements revealed a maximum operating temperature of 592°C. Creep rupture tests were performed at the operational stress, 43 MPa, and at temperatures between 640 and 680°C. The data were extrapolated linearly at a slope parallel to that of the mean data for unused material to predict the remanent life at the service temperature, and an estimation of the life which would be gained by a reduction in the operating temperature. This is illustrated in Figure 1.4. It should be noted that such extrapolation will not take fully into account the microstructural changes during service and therefore the results should be treated with caution.

1.2.2 Metallographic examination of damage

Increasing effort has been put into the assessment of remanent life by direct observation of the steel microstructure. It is therefore necessary to identify what features in the microstructure indicate a departure from the steady strain rate and the onset of tertiary creep. If creep cavitation can be identified as a failure mechanism in a particular component, then quantification of the number density of cavities can be a useful indicator of the remanent life. Some low alloy steels are susceptible to low ductility creep failures in certain microstructural conditions, particularly the coarse grained structures which occur in weld heat affected zones. Others have low ductility in their standard condition. Eventual failure results from the nucleation, growth, and coalescence of cavities on grain boundaries (especially prior austenite grain boundaries). Cavities are often associated with the larger grain boundary alloy carbides, and oxide and sulphide particles. The cavities provide nuclei for microcrack initiation, can locally alter the

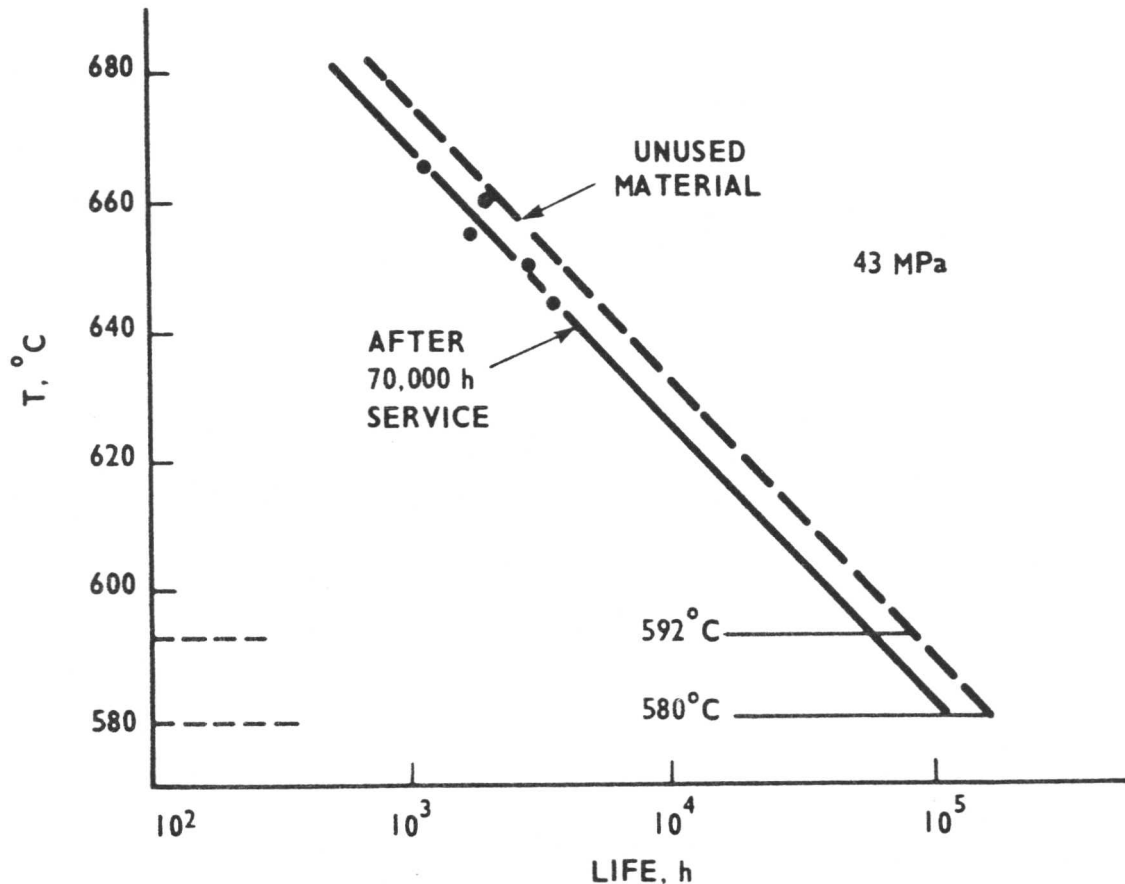


Figure 1.4: Remanent life assessment of $\frac{1}{2}\text{Cr}\frac{1}{2}\text{Mo}\frac{1}{4}\text{V}$ steel reheater drum material by iso-stress post-exposure testing (Cane and Townsend, 1984).

nature of the fracture path and may change the balance of the elements in the solid solution.

Experimental studies have been made (Shammas, 1987) in which the number fraction of cavitated grain boundaries has been measured at various stages throughout a creep test. This fraction is usually termed the 'A' parameter. Assessment of the 'A' parameter is made by taking plastic replicas from a metallographically prepared surface which is subsequently examined with an optical microscope. A sequence of micrographs illustrating the accumulation of creep damage in a $1\text{Cr}\frac{1}{2}\text{Mo}$ steel is shown in Figure 1.5. Initially isolated cavities ($A=0.102$) gradually orientate parallel to the stress axis ($A=0.204$), and then develop into microcracks ($A=0.289$). Macrocracks correspond to a value of $A \approx 0.5$ at which point the component should clearly be removed from service.

In steels of high creep ductility, from which most high temperature components are constructed, significant cavitation does not occur until late in life and is not therefore a useful indicator of remaining life. Effective use of this method of cavitation damage quantification is therefore restricted to weld heat affected zones rather than bulk material.

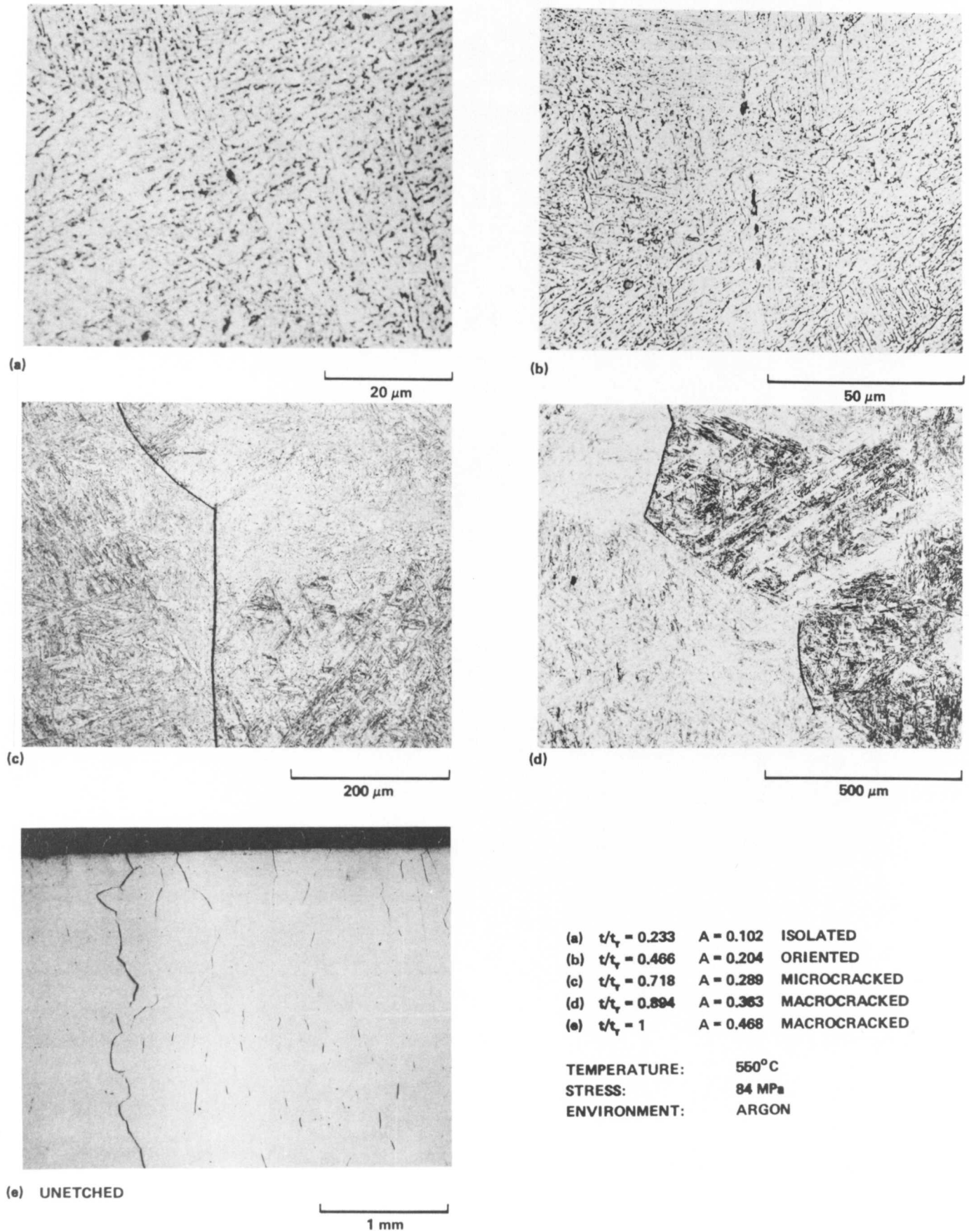


Figure 1.5: Accumulation of creep damage through life of a $1\text{Cr}\frac{1}{2}\text{Mo}$ steel specimen (Shammas, 1987).

1.2.3 Assessment based on plant operational records

An analysis of the past operating history of a component is one of the most important steps in any remanent life assessment procedure. In practice, data taken during plant operation include pressure and temperature measurements, these being logged continuously or taken at fixed times during the day. To calculate a preliminary assessment of the exhausted creep life fraction, the life fraction rule (Robinson, 1938) is used. This states that

$$\sum_i \frac{t_i(\sigma_i, T_i)}{t_{if}(\sigma_i, T_i)} = 1 \quad (1.1)$$

where t_i is the time spent at stress σ_i and temperature T_i , and t_{if} is the failure time at stress σ_i and temperature T_i . It was proposed that for any series of stress and temperature conditions, the life fractions could be linearly summed with final failure denoted by unity. This is a very simple procedure and thus can be used as a first stage of remanent life assessments to establish components requiring further monitoring. For many years the life fraction rule has been used without much consideration of the potential errors.

The failure time, t_{if} , at a particular stress, σ_i , is taken from the International Standards Organisation (ISO) stress rupture data. For any class of material upper and lower bounds have to be placed on the rupture life due to the range of variables such as specimen size and composition variations involved in collecting ISO data. This immediately introduces pessimism into remanent life estimates because it is usually necessary to use the lower bound of the data because it is not possible to identify the actual position of the material within the band without additional creep testing and/or knowledge of virgin material properties. If archive material is no longer available it would be necessary to reheat-treat the service exposed material to recreate the starting microstructure, although it should be noted that for some materials simply repeating the original heat treatment may not restore the material to its original condition. This bandwidth is illustrated for $2\frac{1}{4}\text{Cr1Mo}$ steel at 560°C (based on the stress to give failure in 100,000 hours), the bandwidths being given as a percentage change in the applied stress, in Table 1.2.

Table 1.2: The variation in failure time as a function of the percentage change in the applied stress.

% Change in stress	-20%	-10%	-5%	0	5%	10%	20%
Failure time, hours	38 000	62 000	78 000	100 000	110 000	130 000	200 000

Another problem with the use of standard data is that often they only exist for times of approximately 80,000 hours and so extrapolation to times approaching 150,000 hours is uncertain. This is because during tests the load carrying area is reduced as the specimen extends and by oxidation. Current extrapolation procedures do not take this into account and therefore errors in life estimates occur. The life fraction rule is often used in conjunction with post-exposure testing to determine the failure times at specific stresses, rather than using standard materials data.

The earliest difficulty to be recognised was that when smaller specimens were machined from failed uniaxial creep samples, they had a finite life on retesting, inferring that the life fraction rule is conservative. Alternatively, such results could be interpreted to mean that creep damage is not distributed uniformly within a specimen, being primarily at the point of failure, and thus sampling errors are always present.

To be able to apply the life fraction rule it is necessary to know the representative rupture stress for the component concerned. The key point is that the majority of creep-rupture data are generated under simple uniaxial conditions, whereas in reality components are subject to much more complex loading. It is necessary, therefore, to be able to define a representative stress which, when applied to uniaxial data, adequately characterises the component deformation and failure. The idea of using a reference stress, σ_{ref} , has received much attention in recent years. σ_{ref} for a particular component is defined as that stress which would fail a simple tensile specimen at the same temperature in the same time as the component. When the temperature also varies with time, a reference temperature can be similarly defined at which the comparative specimen test should be performed. Determination of reference stresses and temperatures for irregularly shaped components can now be accomplished by theoretical and experimental work involving computer techniques such as finite element stress analysis together with model and full size component testing. A typical finite element mesh used to calculate the reference stress for a complex pipe geometry is shown in Figure 1.6.

It has been shown that operational stresses and times can be determined accurately and therefore the only unknown for input into the life fraction rule is the exact operating temperature of a particular component. The accuracy of remanent creep life estimates using the life fraction rule depends critically upon the sensitivity of the component material to variations in temperatures. Therefore, careful attention is required when establishing component metal temperatures from operating records. Depending on the direction of heat flow, the metal temperatures may be higher or lower than the steam and may vary significantly with plant operation. The importance of accurate service temperature assessments was emphasized by Cane

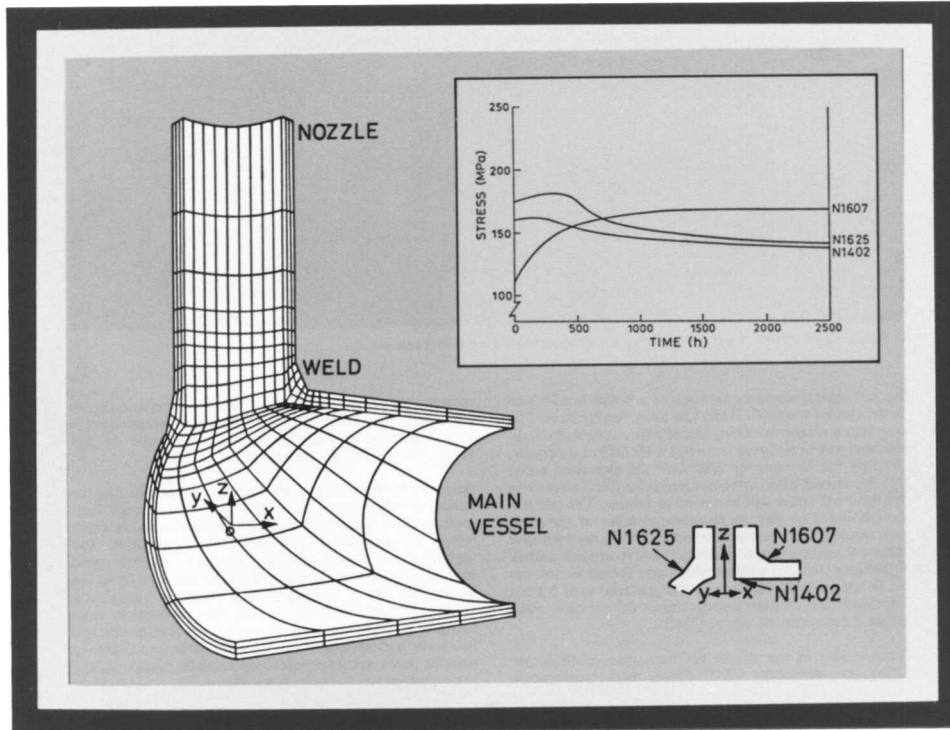


Figure 1.6: A typical finite element mesh used to calculate the reference stress for a complex pipe geometry (Gooch, 1988). The inset shows typical results of a finite element analysis plotted as stress as a function of time at certain critical locations.

and Townsend (1984). They considered in particular the measurement of the temperature of steam headers, and found that errors in the measurement of operating temperature and of the accumulated time–temperature behaviour arose from:

- (1) instrumentation errors,
- (2) spatial variations in the temperature along the header,
- (3) and irregular temperature fluctuations with time as a result of changes in the mode of boiler operation.

The inlet stub tube variation around an 18 tube element on a 500 MW reheater drum is shown in Figure 1.7. It is clear that determination of the metal temperature by measurement of the steam temperature can lead to large errors. For conservatism in the life estimate calculation it is necessary to assume a large ΔT for the metal–to–steam temperature differential, and consequently considerable pessimism is observed in the creep life estimate. The uncertainty may be as high as $\pm 5^\circ\text{C}$.

The effect of temperature on rupture life is illustrated in Table 1.3. This is based on the

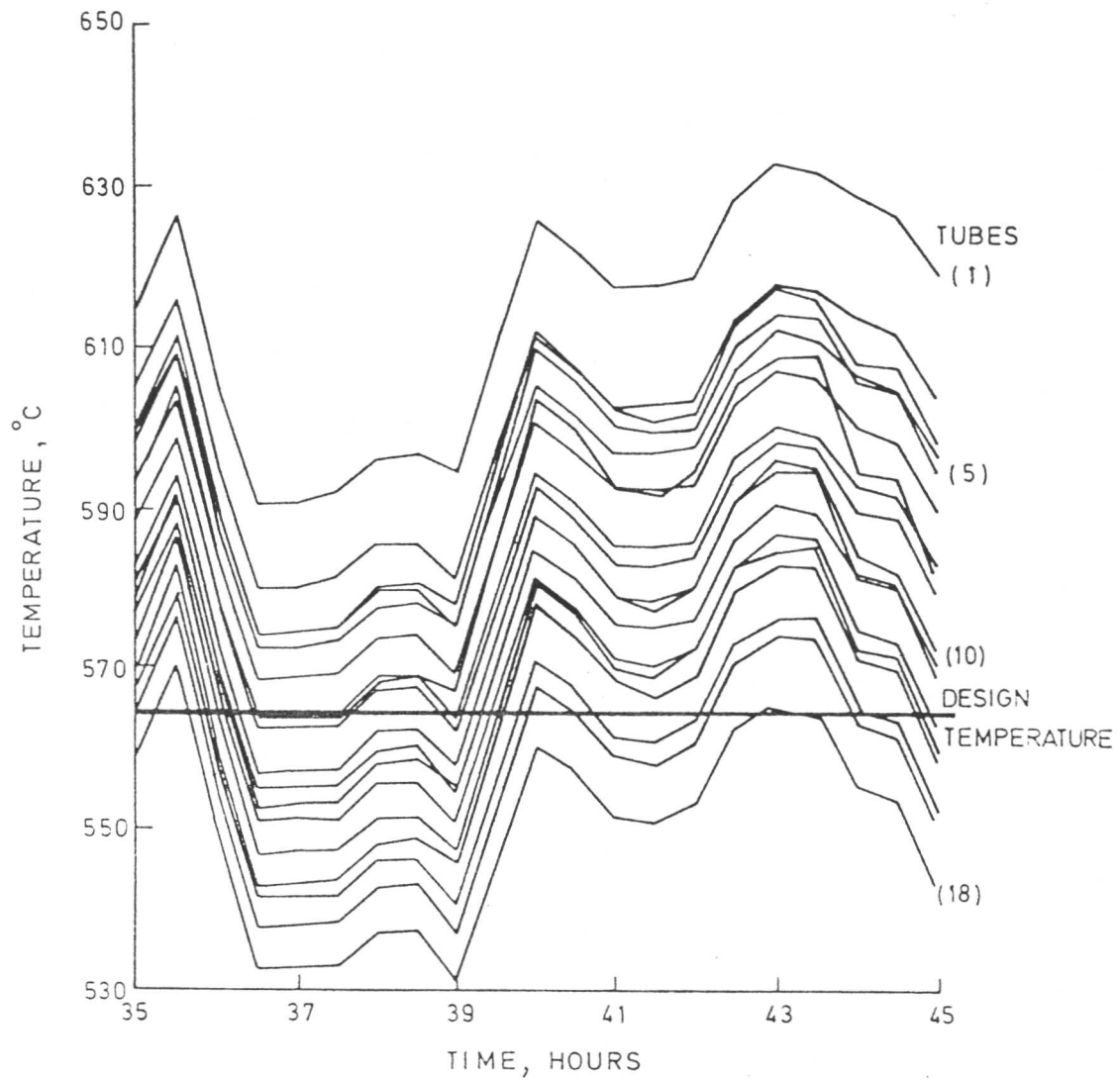


Figure 1.7: Inlet stub tube temperature variation around an eighteen tube element on a 500 MW reheater drum (Cane and Townsend, 1984).

mean stress to give failure in $2\frac{1}{4}\text{Cr1Mo}$ at 560°C in 10^5 hours, and indicates that an error in temperature evaluation of 10°C can lead to variations in the life estimate by a factor of 2.

Table 1.3: The effect of temperature on rupture life.

Temperature /°C	540	550	560	570	580
Failure time /Hours	2.5×10^5	1.7×10^5	1×10^5	56 000	32 000

1.2.4 Estimation of the average thermal history of a component

If it is assumed that fluctuations in temperature and time will produce the same effect as an average temperature over the same total time then it is possible to obtain a better estimate of the remanent creep life by establishing an effective temperature experienced by a component. Detailed microstructural studies can therefore be used to independently support and improve upon the service temperature estimates based on operating records.

The first attempts to relate microstructural changes to the creep life of components were made by Toft and Marsden (1961). They focussed on the spheroidization of carbides in pearlitic and ferritic microstructures of $1\text{Cr}\frac{1}{2}\text{Mo}$ steels. Tubes from a number of power stations which had experienced service for up to 100,000 hours and at temperatures in the range 454–518°C were examined optically. There were a number of difficulties in this work, primarily because all the materials had slightly different base compositions and because the metal temperature histories were not known. Stress rupture tests were carried out at 565 and 510°C for up to 10,000 hours. It was found that there was a clear trend for a decrease in the rupture strength with increasing carbide spheroidization and precipitation of carbides other than cementite. The strength properties were found to be the poorest when the carbide M_6C was present in the microstructure. The detailed microstructural results of this work are presented in Table 1.4.

Toft and Marsden also made the interesting observation that during a large part of the life of the pipes examined there appeared to have been very little creep. Creep only began to occur at a significant rate when the strength properties had decreased as a result of prolonged heating or the wall thickness had been reduced by an appreciable amount. In order to relate the results of the microstructural investigations with operational parameters, the temperature measurement available nearest the pipe removed from service was combined with the operating time of the plant using a conventional time–temperature parameter of the form $t(C + \log T)$, where t is the service time, T the temperature and C a constant, and plotted against the degree of spheroidization observed. A reasonable correlation was found, and it was proposed that an estimate of service temperature could be obtained by classifying the microstructure into one of a number of distinct bands with respect to the degree of spheroidization. This could then be related to the time–temperature parameter, from which the service temperature could be determined. This method is, however, limited by the resolution of light microscopes and the large extrapolation involved.

A number of other attempts have been made to relate precipitate spacing with creep life (Carruthers and Day, 1968; Hale, 1975; Battaini *et al.*, 1990) but these have been met with limited success due to difficulties in characterising complex precipitate distributions. A potentially

Table 1.4: Stages in carbide spheroidization and precipitation in $1\text{Cr}\frac{1}{2}\text{Mo}$ steel superheater tubes (Toft and Marsden, 1961).

Stage	Spheroidization	Precipitation
A	Typical of the structure of a new tube consisting of ferrite and a very fine pearlite.	The carbide present in the pearlite areas is Fe_3C . Evidence of Mo_2C particles beginning to precipitate in the ferrite grains (up to $0.1\ \mu\text{m}$).
B	The first stages of carbide spheroidization usually coinciding with the appearance of small particles of carbides at the grain boundaries.	Small particles of both Cr_7C_3 and Mo_2C (up to $0.2\ \mu\text{m}$) present in the ferrite, (particles of Cr_7C_3 probably also present on the grain boundaries but not yet identified).
C	An intermediate stage of spheroidization, showing more distinct signs of carbide spheroidization in the pearlite areas, but some carbide plates still evident. Increased carbide precipitation within the ferrite grains and at the grain boundaries.	Medium sized particles of Cr_7C_3 and Mo_2C (up to $0.5\ \mu\text{m}$) present in the ferrite.
D	Spheroidization of the carbides is virtually complete, but they are still grouped in the original pearlitic pattern.	Some cementite particles have transformed to Cr_7C_3 . The particles of Mo_2C and Cr_7C_3 in the ferrite have further increased in size (Mo_2C up to $1.5\ \mu\text{m}$).
E	Spheroidization is complete and the carbides are dispersed, leaving little trace of the original pearlite areas.	The pearlite areas have dispersed and the Fe_3C particles have completely transformed to Cr_7C_3 and Mo_2C particles. The Mo_2C and Cr_7C_3 precipitates are large in size (Mo_2C up to $1.5\ \mu\text{m}$).
F	There is a marked increase in the size of some carbide particles, partly due to coalescence.	The pearlite areas are completely dispersed. The amount of Mo_2C present throughout the structure has decreased to form areas of the complex metal carbide M_6C . This metal carbide is Mo rich, but contains both Cr and Fe. Some new grains of ferrite may have been formed.

more powerful method is to investigate the microstructure of the steel in detail with particular reference to carbide composition and type. Carbide composition measurements can now be made routinely using energy dispersive X-ray analysis techniques facilities on transmission electron microscopes. Titchmarsh (1978) demonstrated this method by studying alloy carbides in $2\frac{1}{4}\text{Cr}1\text{Mo}$ steel. He found that each carbide type had a distinct composition with respect to the substitutional alloying elements in the steel. Carbides can be extracted from the bulk material using carbon replication techniques (Smith and Nutting, 1956) which ensures there is no interference from the matrix in measuring the composition of each individual carbide.

Carruthers and Collins (1981) monitored changes in the composition of pearlitic cementite in $\frac{1}{2}\text{Cr}\frac{1}{2}\text{Mo}\frac{1}{4}\text{V}$ and $1\text{Cr}\frac{1}{2}\text{Mo}$ steels using scanning transmission electron microscopy (STEM) and energy-dispersive X-ray analysis as a function of service conditions. They found that the concentration of the substitutional alloying elements Cr, Mo and Mn in the cementite gradually increased with service time at the expense of the Fe content. They therefore proposed that changes in substitutional solute concentration of carbides with time was a viable method for the estimation of the effective temperature experienced by a component. Afrouz *et al.* (1983) then investigated changes in bainitic cementite composition in reheat-treated and service-exposed material in a $1\text{Cr}\frac{1}{2}\text{Mo}$ steel. Afrouz *et al.* confirmed the results of Carruthers and Collins, observing an approximately linear relationship between the changes in concentration of the substitutional solute elements in the cementite and $\text{time}^{\frac{1}{3}}$, which they justified on the basis of diffusion controlled coarsening theory (Christian, 1975). Further work by Du (1986) has provided a large amount of experimental data on composition changes in pearlitic and bainitic cementite; however, no physical explanation of the composition changes was put forward.

A firm theoretical basis is needed in order to model the diffusion processes resulting in the composition changes in the cementite. Bhadeshia (1989) has developed a model to predict the rate at which the alloying elements redistribute between ferrite and cementite, subject to the thermodynamic constraints which determine the equilibrium amount of alloy in the two phases. The model uses a finite difference method to find numerical solutions to the diffusion equation. (Due to the irregular distribution and varying sizes of the cementite particles it would be very difficult, if not impossible, to obtain analytic solutions to the diffusion equation.) The model so far has highlighted the factors controlling the approach to equilibrium. In particular, particle size has been found to have a strong influence on the rate at which cementite composition changes. Reasonable agreement has been found with experimental data to date. However, the model contains a number of simplifications. It assumes that diffusion occurs only in one dimension, that particle size does not change during enrichment, that the diffusion coefficient of the substitutional alloying elements in ferrite is the same as in cementite, that local equilibrium is maintained at the interface during diffusion and interaction between the diffusing elements is neglected. The aim of this work is to test the assumptions of this model, and develop it further to overcome some of its limitations. Experiments are performed on a variety of steels using many different techniques to verify and assist with the development of the model.

1.3 Possible future indicators of thermal history

It has recently been suggested that small amounts of additional material, 'plugs', could be attached to power plant in order to estimate the average thermal history of critical components. These plugs have specific advantages over thermocouples in that they are fixed directly to the metal, eliminating any metal-steam temperature differentials, and that they can be manufactured into convenient shapes such as bolts or clips for ease of attachment to the components being assessed. Peak temperature indicators have also been tested. These consist of a material of a suitable known melting point which melt when the temperature exceeds the working limits. Peak temperature indicators are not suited to situations where there are periodic small excursions above and below the service temperature in power plant.

The first commercial 'plug' was developed by Shell Research Ltd. and made use of hardness changes in metals and alloys as a function of high temperature heat treatment. However, the questionable reliability of portable hardness testers has led to the introduction of a new device. The newest indicator of thermal history developed by Lai *et al.* (1990), subject to Patent Application 8918774.4, is made from a duplex stainless steel which contains austenite and ferrite. The device relies on the fact that austenite gradually decomposes to ferrite, carbides and intermetallics on annealing at high temperatures. A simple on-site measurement of the magnetic permeability of the 'plug' can be used to determine its ferrite content, ferrite being ferromagnetic and austenite not. The measured ferrite content can then be used, in conjunction with the initial ferrite content and the operating time, to determine the average thermal history of the material to which the 'plug' is attached. The effect of thermal excursions about the operating temperature on the transformation characteristics of the duplex stainless steel are currently being investigated.

1.4 Conclusions

Over recent years much work has been done within the power generation industry on developing a reliable and accurate methodology for estimating the remaining creep life of high temperature components. It has been shown that techniques based on the measurement of operational parameters and the use of the life fraction rule give poor accuracy and are generally pessimistic due to conservatism in assessing the input data. Much greater accuracy can be achieved by direct access to the component for post and during service measurements and sampling.

Continuing research and development is needed to improve remanent life estimates, particularly on more sensitive post service inspection methods. The focus of this work therefore not

to study the factors conferring creep resistance on power plant steels, but to model theoretically and verify experimentally changes in carbide composition, size and identity, so that the steel microstructure can be used as a **time-temperature recorder**. A more accurate assessment of the thermal history experienced by a component can then be used, together with stress measurements, to predict the remaining life of a particular component ensuring the safe and economic extension of high temperature plant service beyond present, generally conservative, design limits.

CHAPTER 2

PHYSICAL METALLURGY OF ALLOYED STEELS

This chapter contains a review of the physical metallurgy of alloyed steels. This is important in that changes occurring in carbide composition, identity, size and shape are put into the context of the different matrix microstructures in which they occur.

CHAPTER 2

PHYSICAL METALLURGY OF ALLOYED STEELS

2.1 Introduction

When the high temperature face-centred cubic (f.c.c.) phase, austenite, in steel decomposes to the less dense body-centred cubic (b.c.c.) phase, ferrite, a number of different microstructures and morphologies can form which depend on the cooling rate, the presence of alloying elements, and the conditions and availability of lower energy nucleation sites for heterogeneous nucleation.

2.1.1 The distribution of alloying elements in steels

In steels in which the austenite transforms to ferrite and carbides on slow cooling, the role of the alloying elements can be split into three categories. Firstly, there are elements which are normally found mostly in the ferrite phase such as Ni, P and Si, their solubility in cementite or in alloy carbides being quite low. Secondly, there are elements which can both form stable carbides and can be found in solid solution within the ferrite. Typical elements which exhibit this type of behaviour are Mn, Mo, Cr, V, W, Ti and Nb. The amount of each needed in its carbide depends on the carbon content of the steel; however, they are usually present in excess of this amount, with the remainder going into solid solution in ferrite. There are also some elements which primarily enter the carbide phase. Nitrogen is the main example of this behaviour, readily forming carbo-nitrides with iron and many alloying elements, and separate alloy nitride phases in the presence of titanium or aluminium, for example.

2.1.2 The effect of alloying elements and cooling rate on the γ/α transformation

The different tendencies of alloying elements to exist in ferrite or carbides result in the rate at which the decomposition of austenite occurs below A_{e_1} being sensitive to their concentrations in the steel. (A_{e_1} is the temperature of the eutectoid reaction.) Also increases in undercooling and the cooling rate from austenite limit the ability of alloying elements in iron, and the iron atoms themselves, to diffuse during the transformation to the equilibrium structure, and increases the likelihood of the formation of metastable structures.

The alloying elements are divided into two types, those in substitutional and those in interstitial sites. Substitutional elements (e.g. Cr, Mo etc.) occupy lattice sites within the iron lattice and require vacant sites in order to diffuse, whereas interstitial elements (e.g. C, N) can diffuse much more quickly, occupying and moving between interstices within the iron lattice. Diffusion of the interstitials can only be suppressed at high undercoolings. The reaction

process can be controlled by either of these diffusing species. In the case of diffusion of the substitutionals being dominant, it is found that growth occurs with partition of the element between α and γ under local equilibrium conditions. The ferrite grows at a slow rate determined by the diffusivity of the alloying element within the austenite. It is in fact more common for a reaction to be controlled by the diffusion of carbon (interstitial), in which case growth occurs with no partitioning of the alloying element. The observed growth rates, since they are controlled by the diffusivity of carbon, are relatively high. It is also possible to have a diffusionless transformation. Whether the reaction process and rate is controlled by either diffusion of interstitials or substitutionals, or is diffusionless, is determined by a combination of thermodynamic and kinetic constraints. Hence, both the cooling rate and alloy content are critical to the development of a particular microstructure.

The possible morphologies which can be produced are discussed in detail in the next section. This includes a brief discussion of the formation of allotriomorphic and idiomorphic ferrite, Widmanstätten ferrite, and more detailed discussion of the formation of bainite and martensite, because it is within these two microstructures that changes in carbide compositions are monitored.

2.1.3 Diffusional transformations—The reconstructive growth of ferrite

The f.c.c. lattice of austenite can undergo a reconstructive transformation to the b.c.c. ferrite if there is little undercooling and diffusion can occur. This can be thought of in the manner illustrated in Figure 2.1.

Diffusional ferrite in steels nucleates heterogeneously and is observed to grow in two forms, allotriomorphic and idiomorphic ferrite. The term allotriomorphic is used when the ferrite has a shape which does not reflect its crystal symmetry. Allotriomorphic ferrite nucleates at prior austenite grain boundaries and then grows preferentially along the grain boundary, where diffusivities are high, as illustrated in Figure 2.2.

Idiomorphic ferrite, however, has a shape which is related to its crystal structure. It nucleates and grows intragranularly, generally taking the form of equiaxed grains.

2.1.4 Widmanstätten ferrite

If undercooling occurs slightly below the A_{e_3} temperature for a particular alloy, the increase in free energy driving force for the reaction and the decrease in atomic mobility result in the formation of Widmanstätten ferrite. (The A_{e_3} temperature is the temperature at which austenite transforms to ferrite. For pure iron this occurs at 910°C, but transformation occurs at progressively lower temperatures as the carbon content of the steel is increased.) Diffusion

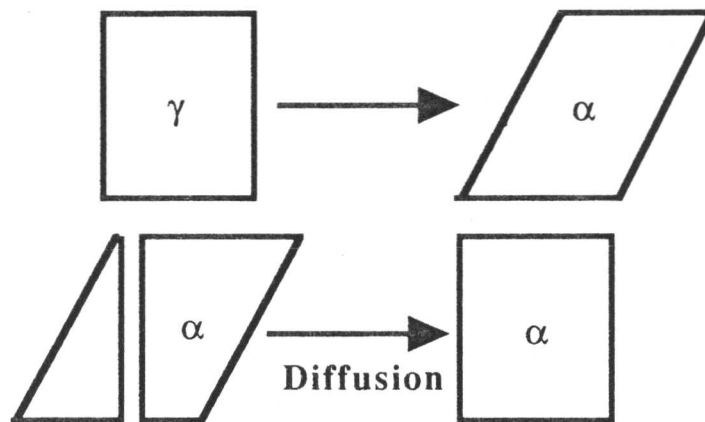


Figure 2.1: The reconstructive growth of ferrite.

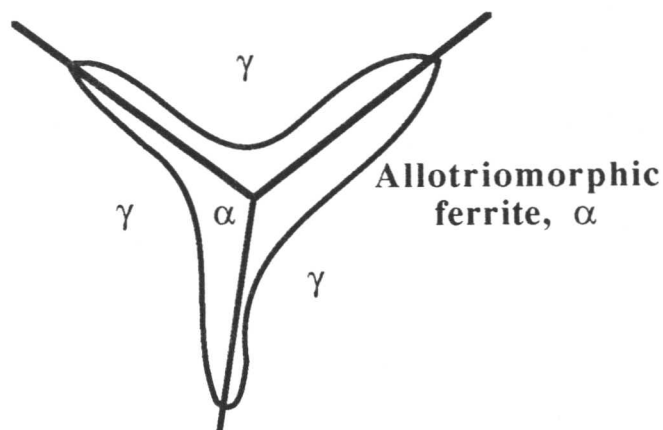


Figure 2.2: The growth of allotriomorphic ferrite along grain boundaries.

of carbon is a thermodynamic necessity and Widmanstätten ferrite forms with the equilibrium carbon concentration, therefore with carbon partitioning during the transformation. Growth is accompanied by an Invariant-Plane Strain (IPS) shape change, and there is no diffusion of substitutional solute or iron atoms. (A deformation which leaves a plane undistorted and unrotated is called an invariant-plane strain.) At these temperatures the available driving force is much less than the strain energy due to the shape change, and so to accommodate this strain energy, growth involves the simultaneous formation of two plates, appearing under an optical microscope as one, although they have different habit planes with respect to the parent austenite. The growth rate has been shown to be determined by carbon diffusion rates in the austenite at the glissile α_w/γ interface (Bhadeshia, 1981). This is illustrated in Figure 2.3.

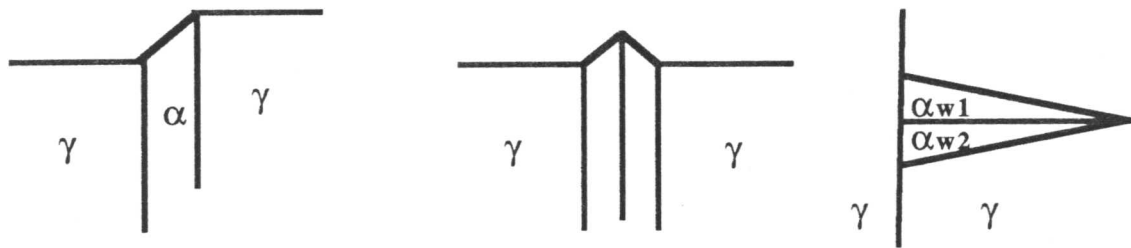


Figure 2.3: The growth of Widmanstätten ferrite planes.

2.2 Bainite

Bainite is a non-lamellar mixture of ferrite and carbides which is formed by the decomposition of austenite at a temperature above the martensite start temperature, M_s , but below the temperature at which pearlite can form. It has been shown that during the diffusionless formation of martensite there is a physical change in the shape of the parent phase, whereas a diffusional reaction requires mass transport to produce a change in structure without introducing strains (Bhadeshia, 1985). The bainite transformation, being intermediate between the diffusionless martensite and diffusional pearlite reactions has presented difficulties in interpretation in the past (Aaronson, 1986), although these are now beginning to be resolved (Christian and Edmonds, 1984; Bhadeshia, 1988; Bhadeshia and Christian, 1990).

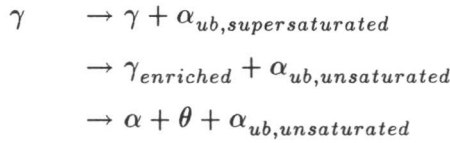
2.2.1 Morphology and carbide precipitation

Bainite consists of non-lamellar aggregates of ferrite and carbides, the ferrite being in the form of thin plates approximately $10 \mu\text{m}$ long and $0.2 \mu\text{m}$ thick, commonly referred to as sheaves (Hehemann, 1970). The growth of the sheaves is limited by hard impingement with the austenite grain or twin boundaries, and they have a relatively high dislocation density. Carbides are not an essential feature of bainite, and in fact they are completely absent in many cases. In particular, in alloys containing high concentrations of Si or Al, Fe_3C precipitation is so slow that to all intents and purposes the bainite consists only of bainitic ferrite and retained austenite.

The formation of bainitic ferrite leads to an increase in the carbon concentration of retained austenite. There are two different morphologies associated with bainite formation. Upper bainite forms at the higher temperatures within the range, the cementite precipitating from

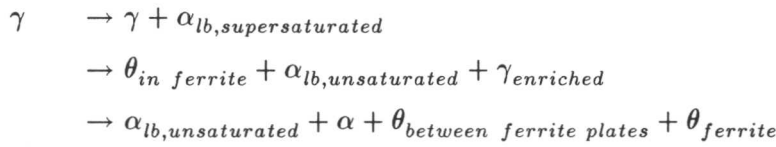
films of carbon-enriched austenite which separate the plates of bainitic ferrite. The platelets within a sheaf are all in the same orientation in space and the orientation between α_b and γ is the same as for α'/γ . In lower bainite, however, cementite also forms within the platelets of ferrite. In contrast to the cementite obtained after tempering supersaturated martensite, the carbides formed within any given lower bainitic plate usually occur in a single crystallographic orientation (Bhadeshia, 1988). There are therefore two kinds of cementite particles, those growing from carbon-enriched austenite and those precipitating from supersaturated ferrite. The precipitation of cementite generally occurs as a secondary reaction after the growth of bainitic ferrite (Hehemann, 1970). The precipitation sequences are summarised below.

1. Upper bainite

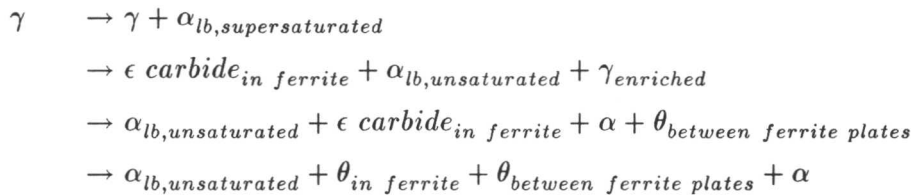


2. Lower bainite

a. High dislocation density



b. Low dislocation density



The two different morphologies of bainite are illustrated in Figure 2.4.

2.2.2 The shape change associated with the transformation

Bainite growth is also associated with an IPS shape change (Ko and Cottrell, 1952), as is the martensite reaction. The origin of this IPS shape change has been one of the prime areas of dispute in the proposed theories for the bainite reaction mechanism. It has been established (Bhadeshia and Waugh, 1982; Stark *et al.*, 1987) that iron and substitutional atoms do not diffuse during the reaction. Various observations imply that the formation of bainite involves the co-ordinated movement of the substitutional solute and iron atoms across a glissile transformation interface. These include the fact that the shape change gives rise to an elastically accommodated stored energy in the sheaves in the region of 400 J mol⁻¹. The high temperatures associated with the transformation result in the yield strength of both phases

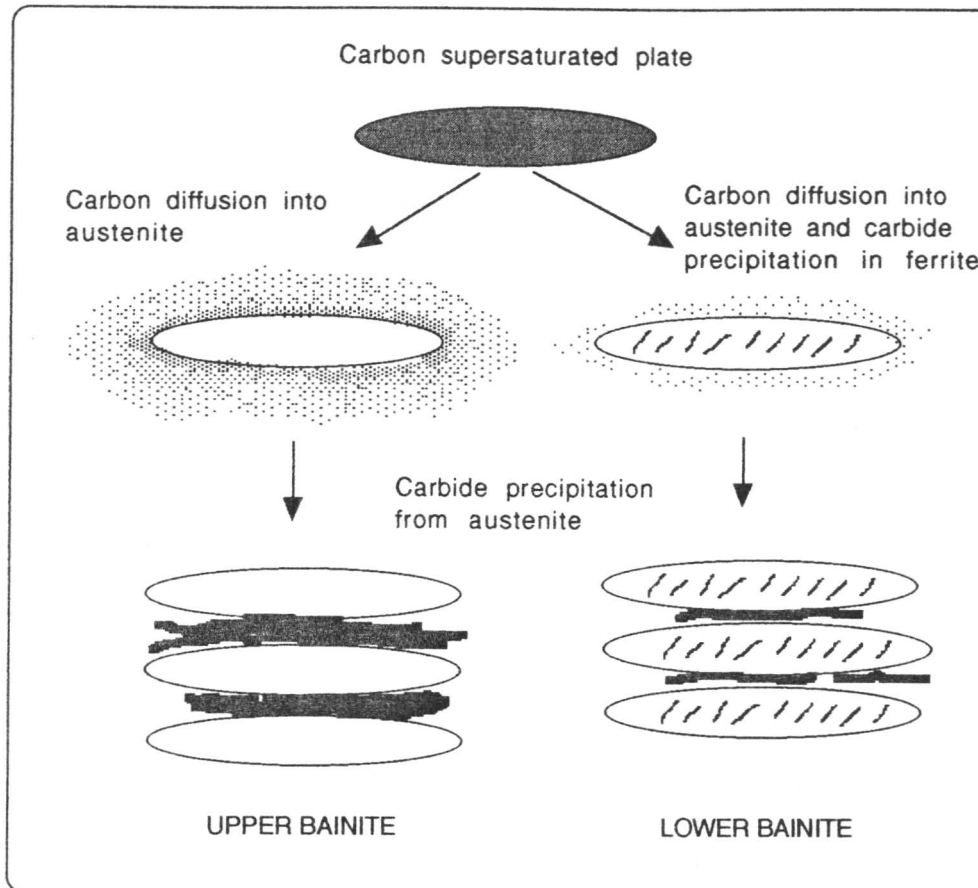


Figure 2.4: The morphologies of upper and lower bainite.

being comparatively low, and so plastic deformation can occur. The high dislocation density induced by attempts to relieve some of this strain is then responsible for hindering the advance of the transformation front, and thus limiting the size of the bainite sheaves (Bhadeshia and Edmonds, 1979). This can explain the observed limit on the growth of bainite in the absence of hard impingement. The ferrite plates always have a crystallographic orientation relationship with γ which is similar to that found between γ and α' . This type of co-ordinated movement cannot generally be sustained across randomly oriented grains, and so bainite growth is impeded by austenite grain boundaries. This is in contrast to diffusional transformations in which the product phase may readily grow across grains of the parent phase which are in different orientations.

It has been suggested (Kinsman *et al.*, 1975) that an IPS shape change can occur when a sessile semi-coherent interface is displaced by the motion of incoherent steps. However, there is no mechanism to explain how the systematic displacements implied by an IPS can

be caused by the unco-ordinated transfer of atoms across the steps. It should also be noted that allotriomorphic ferrite grows by a step mechanism, and despite it having the necessary semi-coherent interface, it does not show an IPS surface relief. The atomic correspondence implied by the shape deformation must be a property of a particle as a whole, rather than being dependent on interface orientation (Christian and Edmonds, 1984), also contradicting the above hypothesis.

2.2.3 The role of carbon in the bainite transformation

The precise role of carbon during the bainite transformation is difficult to determine (Christian and Edmonds, 1984; Bhadeshia, 1988). Bainite must always form below the T_0 temperature, at which α and γ of the same composition have the same free energy, which can be shown to make it thermodynamically possible for the transformation to be diffusionless. It is also possible to have a paraequilibrium transformation in which the substitutional lattice is configurationally frozen, but the carbon redistributes to equalise the chemical potential in all phases. An intermediate degree of partitioning is also possible. This is illustrated in Figure 2.5.

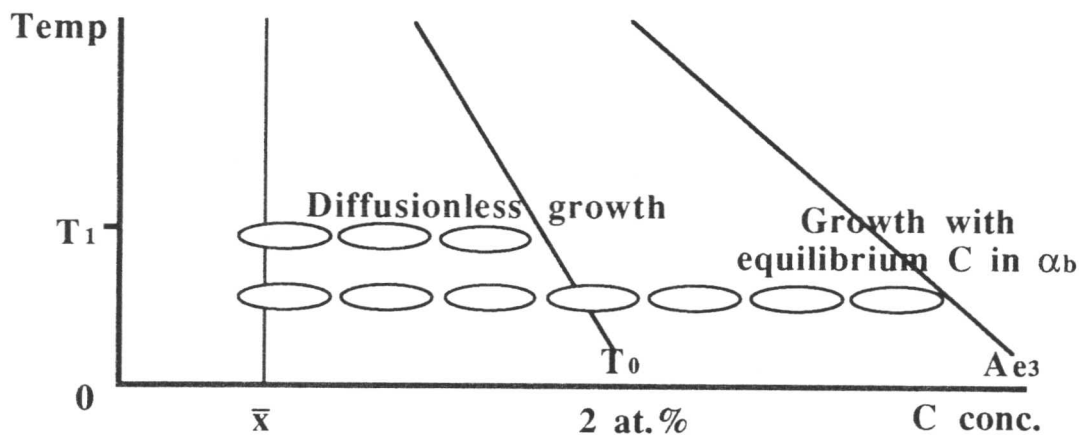


Figure 2.5: Bainite growth mechanisms.

If growth involves diffusionless transformation then any excess carbon in bainitic ferrite can partition into the retained austenite within a fraction of a second after the transformation because of the high diffusivity of interstitial carbon. It is not possible to determine directly the carbon concentration of the ferrite during its growth. The bainite reaction is found to stop before the carbon concentration of the retained austenite reaches that of the equilibrium or paraequilibrium phase boundary, i.e. when diffusionless transformation of carbon-enriched

austenite becomes thermodynamically impossible. The extent of the reaction is a function of temperature, increasing as the temperature is reduced. It is possible to extrapolate to find a bainite start temperature, B_s , above which bainite is not observed to form. This is known as the *incomplete reaction phenomenon*, in which the degree of transformation to bainite is always far less than that demanded by equilibrium.

Bhadeshia (1987) summarises the bainite reaction as a displacive transformation in which there is no diffusion of substitutional or iron atoms across the transformation interface. The excess carbon trapped in bainitic ferrite is removed by a combination of diffusion into the residual austenite, and by the precipitation of carbides between the ferrite. The retained austenite eventually decomposes by a diffusional transformation into a mixture of more carbides and ferrite. The plate morphology of bainite is explained by the minimisation of strain energy due to the IPS shape change associated with the displacive mechanism of the transformation. The kinetics of bainite are also shown to be consistent with the proposed diffusionless, displacive transformation mechanism.

2.3 Martensite

Martensite forms at the highest undercoolings, when the free energy change for the transformation is very large. Hence, rapid quenching of austenite to room temperature results in martensite, a very hard brittle structure in which carbon, originally in solid solution in austenite, remains in solution. Unlike the formation of ferrite or pearlite, the martensite reaction is a diffusionless shear transformation which is highly crystallographic in character and leads to a characteristic lath or lenticular microstructure.

The addition of alloying elements to a steel can affect the temperature, M_s , at which the martensite reaction can begin on cooling the parent phase. The extent to which the reaction proceeds depends on the undercooling below this temperature. Note that martensite can form at very low temperatures where atomic mobility is almost negligible because the transformation is diffusionless. The growth rate can be very high, limited by the speed of sound in the material concerned.

The fact that martensite can form at very low temperatures also means that any process which occurs during its formation also cannot depend on thermal activation, e.g. the interface between martensite and the parent phase must be able to move easily at very low temperatures. For the interface to have high mobility and velocity at low temperatures, it must be semi-coherent or fully incoherent (Christian and Knowles, 1981). It should be noted that fully coherent interfaces are only possible when the two lattices can be related by an IPS. In the γ/α

transformation the austenite lattice cannot transform to a b.c.c. martensite lattice by an IPS only (it occurs by the so-called Bain strain combined with a suitable rigid body rotation and a lattice invariant deformation which is either twinning or slip) and, therefore, the lattices are joined by semi-coherent interfaces. For the γ/α' interface to be glissile it must contain at least one invariant line along which interface dislocations lie.

The interface between the martensite and the parent plate is usually called the 'habit plane'. If the transformation is unconstrained, the habit plane is macroscopically flat, whereas in a constrained transformation it grows in the shape of a thin lenticular plate or lath, resulting in the interface being curved on a macroscopic scale. This is illustrated in Figure 2.6.

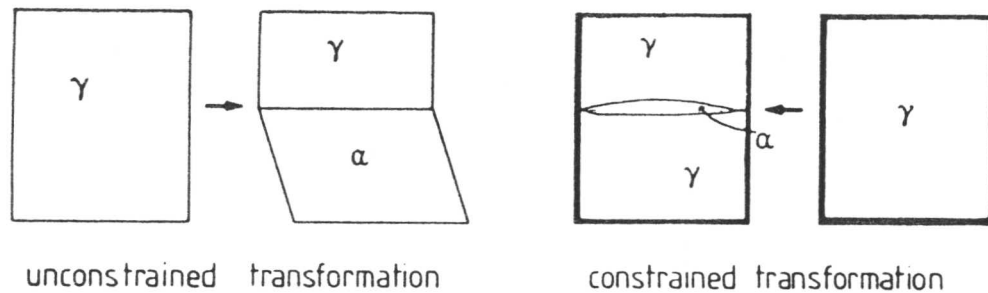


Figure 2.6: Unconstrained and constrained growth of martensite.

There are two kinds of martensite, a plate and a lath morphology. The extent of the martensite reaction has been found to be virtually independent of time. The volume fraction of martensite, f , formed as a function of undercooling below M_s is given by

$$1 - f = \exp[-0.011(M_s - T)] , \quad (2.1)$$

where T is the temperature to which the sample has been cooled below M_s . Since there is no diffusion during the martensite transformation, there will be reproducible orientation relationships between the parent and product lattices. The orientation relationship usually consists of approximately close-packed planes, and with corresponding close-packed directions also being approximately parallel e.g. Kurdjumov-Sachs

$$\{111\}_\gamma \parallel \{011\}_{\alpha'} \text{ and } \langle 10\bar{1} \rangle_\gamma \parallel \langle 11\bar{1} \rangle_{\alpha'} . \quad (2.2)$$

2.3.1 The shape deformation due to the martensitic transformation

When martensite grows there must be a change in shape because the pattern of atomic arrangement changes on transformation and the transformation is diffusionless, the change of shape being caused by the migration of interface dislocations. This is illustrated in Figure 2.7.

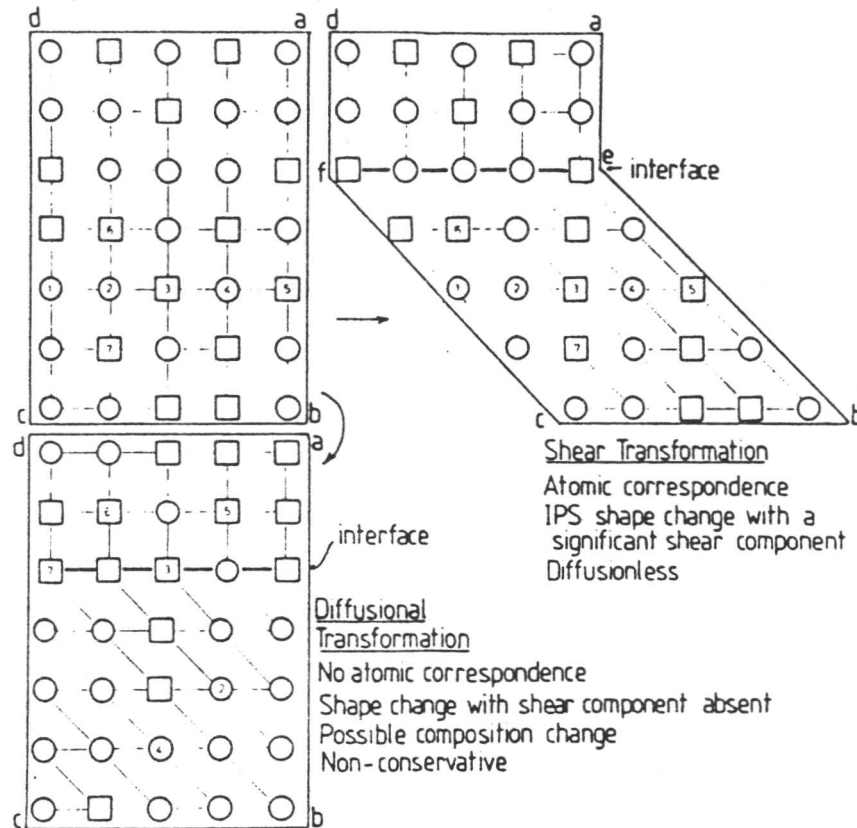


Figure 2.7: Diffusional and diffusionless transformations (Bhadeshia, 1987).

A comparison is made between diffusional and diffusionless transformations, the strain being an IPS and a fully coherent interface existing between the parent and product lattices. The occurrence of the shape deformation in martensite growth therefore implies there is an atomic correspondence between the parent and product lattices. It has been shown that in a constrained environment there is a distortion of the parent lattice around the martensite. The strain energy per unit volume is given by

$$E = \frac{c}{r}(s^2 + \delta^2)\mu, \quad (2.3)$$

where $\frac{c}{r}$ is the thickness/length ratio of the plate, μ is the shear modulus of the parent phase and s and δ are the shear and dilatational components of the shape deformation strain. This explains the plate morphology of martensite, for which E is minimised.

2.3.2 Martensite crystallography

It has been shown that the major feature of the martensite transformation is its shape change, macroscopically having the characteristics of an *invariant-plane strain*. There is an anomaly here because it is found that the Bain strain when combined with an appropriate rigid body rotation gives an *invariant-line strain*, which when applied to the f.c.c. lattice generates the martensite lattice. The Bain strain is illustrated in Figure 2.8.

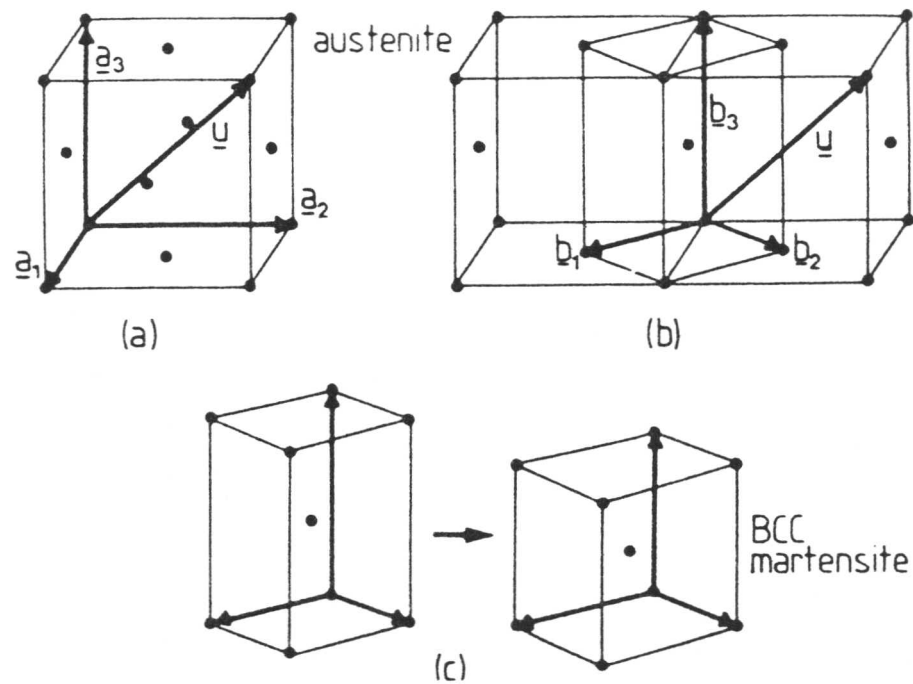


Figure 2.8: The Bain strain to transform austenite to martensite (Bhadeshia, 1987).

This is explained systematically in Figure 2.9. Figure 2.9 a) represents the shape of the initial f.c.c. austenite crystal. On martensitic transformation its shape alters to that in Figure 2.9 b) via an IPS. This is now an intermediate lattice which is not b.c.c., (an IPS on its own cannot convert f.c.c. \rightarrow b.c.c.). An invariant line strain (ILS) can, however, transform f.c.c. to b.c.c. and since an ILS can be factorised into two IPSs, it follows that the further deformation

needed to change the intermediate structure to the b.c.c. structure is another IPS. This now gives the correct lattice change but the wrong shape change. If another deformation is applied which alters the shape but without altering the crystal structure, i.e. is lattice invariant, this brings the experimental observations into agreement with theory. There are two possibilities for the lattice invariant deformation, twinning and slip.

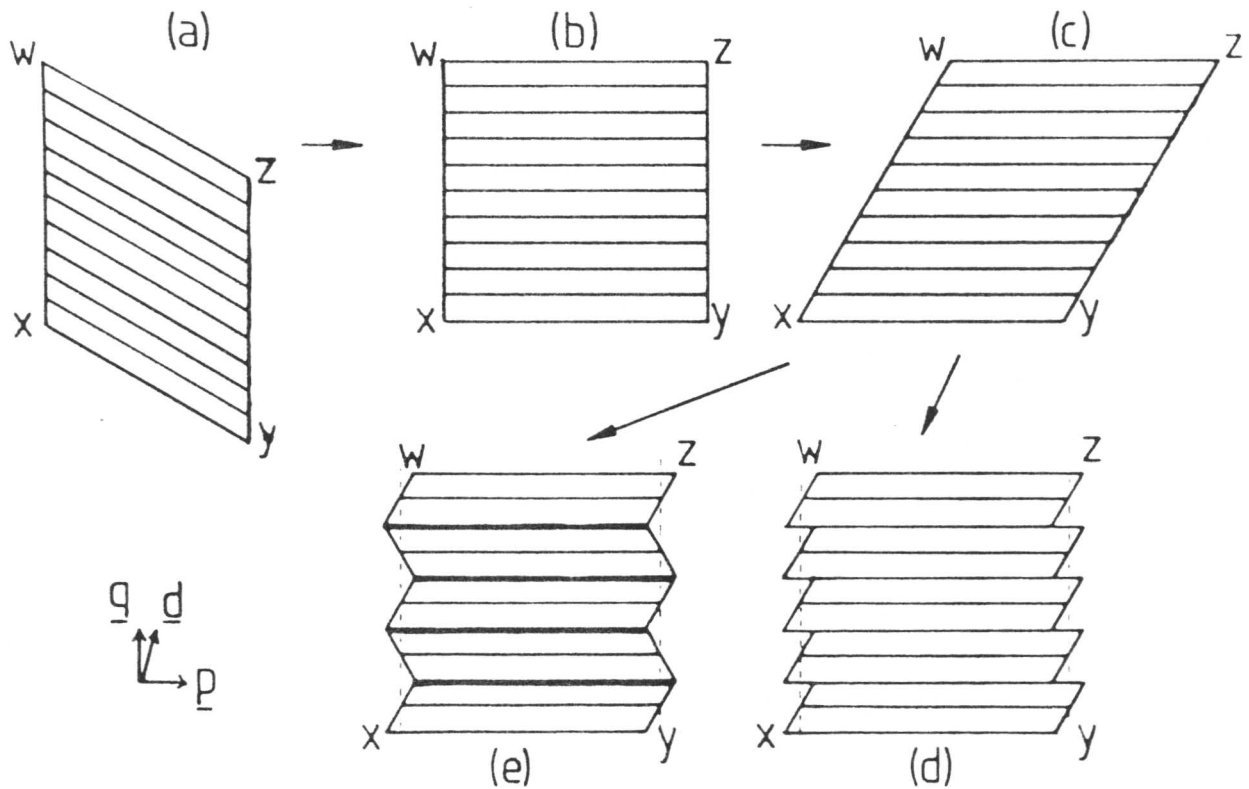


Figure 2.9: The formation of martensite (Bhadeshia, 1987).

This theory therefore explains the apparent contradiction that the lattice transformation strain is an ILS, but that the macroscopic shape deformation is an IPS, and also the experimentally observed transformation twins, and the peculiar habit plane indices, determined by the amount of lattice-invariant deformation.

2.3.3 The tempering of martensite

The presence of martensite in a quenched steel greatly improves the hardness, but it is normally very brittle and so almost all technological steels have to be heat treated to increase their toughness. Tempering is therefore normally carried out in the range 150–700°C. Martensite is a highly supersaturated solid solution of carbon in iron which, on tempering, rejects carbon

in the form of finely divided carbide phases. The microstructure after tempering is a fine dispersion of carbides in a ferrite matrix which often bears no resemblance to the as-quenched martensite. If the martensite reaction does not go to completion on quenching, there will also be some retained austenite which does not remain stable during the tempering process.

It is possible to define four distinct, but overlapping stages in the tempering of ferrous martensites, the discussion being initially restricted to plain carbon steels.

2.3.3.1 Stage 1: up to 250° C

Interstitial carbon atoms in martensite in steels of 0.3–1.5 wt.% C can diffuse within the tetragonal lattice at room temperature, increasing as the temperature is raised to 250°C. The primary stage of tempering is therefore the precipitation of close-packed hexagonal epsilon carbide, ϵ (composition $\text{Fe}_{2.4}\text{C}$) within the martensite. ϵ carbide precipitates as narrow laths on the cube planes of the matrix with a well-defined orientation relationship. It is also possible that cementite will be precipitated, but this will depend on the temperature and composition of the steel. After precipitation of ϵ carbide the martensite is still tetragonal, but has a much lower carbon content (low-carbon martensite). The microstructure at the end of the first stage of tempering consists of retained austenite, low-carbon martensite, and ϵ carbides.

2.3.3.2 Stage 2: 230–300° C

During the second stage the retained austenite decomposes. There is little experimental evidence, but it is thought that bainitic ferrite and cementite are formed. The reaction will only be important if there is an appreciable amount of retained austenite present, e.g. in medium or high carbon steels.

2.3.3.3 Stage 3

During the third stage of tempering cementite (Fe_3C) appears. The reaction commences as low as 100°C and is fully developed by 300°C, the particles being up to 200 nm long and approximately 15 nm in diameter. The most likely sites for the nucleation of the cementite are the ϵ carbide interfaces with the matrix; as the cementite grows the epsilon carbide will disappear. Nucleation and growth of the cementite can also occur on the twins occurring in the higher carbon martensites, with colonies of similarly oriented lath-shaped particles, distinguishable from the usual Widmanstätten distribution of rods. The matrix will no longer be tetragonal, being mainly ferrite saturated with carbon.

2.3.3.4 Stage 4

No further phase changes will occur as tempering proceeds, however the microstructure and mechanical properties will continue to alter. Hyam and Nutting (1956) suggest that the

coarsening and eventual spheroidisation of cementite particles constitutes a fourth stage of tempering. The final result in plain carbon steels is an equi-axed array of ferrite grains with coarse, spheroidised cementite particles, often in the grain boundaries.

2.3.3.5 Alloying elements

The tempering of martensite in an alloyed steel is clearly different than in a carbon steel, because the alloying elements generally move TTT (Time–Temperature–Transformation) curves to longer times. This results in a higher hardenability, because martensite structures can be achieved at slower cooling rates. Alloying elements can also depress the M_s (martensite start) temperature. The main difference in the tempering process is the replacement of cementite by alloy carbides.

The alloying elements will also have an effect on the formation of iron carbides. For example, Si can stabilise ϵ carbide so that it will still be present after tempering at 400°C in steels with 1–2 at. % Si, suggesting that Si enters the carbide structure. In steels containing Cr, Mo, W, V, Ti, Si etc. the tetragonality of martensite can be preserved up to 500°C, the alloying elements increasing the stability of the supersaturated Fe-C solid solution. Alloying elements can also slow down the coarsening of cementite in the range 400–700°C. The most important effect is that many elements (e.g. Cr, Mo, V, W and Ti) form carbides which are thermodynamically more stable than cementite.

Therefore, when strong carbide forming elements are present in a steel, their carbides will be formed in preference to cementite. Many alloy carbides do not usually form until 500–600°C, higher temperatures being necessary for the diffusion of the alloying elements prior to their nucleation and growth. There is often an associated marked increase in the strength of the steel, the phenomenon being termed secondary hardening, in which a relatively coarse cementite dispersion is replaced by a much finer alloy carbide dispersion.

2.4 Summary of transformation mechanisms

The characteristics of the formation of allotriomorphic ferrite, bainite and martensite have been discussed in the previous sections. This section summarises the mechanisms of these transformations. Figure 2.10 illustrates schematically the composition variation expected in the vicinity of the transformation interface. In the case of a reconstructive transformation the compositions of the two phases at the interface are defined by a tie-line of the phase diagram. In a binary alloy, the tie-line passes through the average alloy composition, however, for a ternary system it is not possible to satisfy the mass-balance condition for the three elements simultaneously. There are two possibilities. Firstly, to choose a tie-line which ensures that

the carbon composition in austenite at the interface is almost the same as that in the bulk alloy. This reduces the driving force for carbon diffusion almost down to zero and there will be a concentration gradient of substitutional solute ahead of the interface, implying extensive partitioning and a relatively slow growth rate. This is termed *partitioning local equilibrium* (P-LE). The second possibility is to choose a tie-line for which the concentration of substitutional solute in the austenite is approximately the same as that in the bulk alloy, resulting in a small amount of partitioning and a relatively fast growth rate. This is termed *negligible partitioning local equilibrium* (NP-LE).

In the NP-LE mode the concentration of solute remains the same everywhere except for a 'spike' at the interface, the width of the spike corresponding to the extent of the diffusion field. As the alloy is transformed at progressively lower temperatures the diffusion field gets smaller than atomic dimensions and local equilibrium breaks down. The substitutional element is then trapped across the advancing interface, although carbon is still mobile. This is termed *para-equilibrium*. In the case of martensitic transformations, neither the carbon or the substitutional solute atoms diffuse.

2.5 Carbide precipitation

In steels, pure binary carbides do not generally occur because there is always some solubility of the alloying elements in the various carbide phases, and in many cases solubilities are extensive. It is usual to denote a carbide by a general formula of the form $M_{23}C_6$, where M indicates a mixture of metal atoms. Much information on the composition, structure, morphologies and orientation relationships of various carbides has been obtained, usually with respect to specific steels (*e.g.* Goldschmidt, 1948; Kuo, 1953; Shaw and Quarrell, 1957; Baker and Nutting, 1959; Woodhead and Quarrell, 1965; Jack and Jack, 1973; Yakel, 1985).

Alloy carbides can form in a variety of ways. Sites for carbide precipitation include dislocations from the original α' structure, and at grain boundaries and sub-boundaries (which are energetically favourable sites, providing high diffusivity paths for the rapid diffusion of solute). In many cases the first alloy carbide to form is not the equilibrium carbide, leading to precipitation sequences as the first carbide is gradually replaced by more stable ones. There has been some controversy in past literature as to whether more stable alloy carbides nucleate 'in situ' or separately from the dissolving carbides. Transformations between particular carbides are discussed in the next section.

2.5.1 M_3C

Cementite containing no alloying element additions, Fe_3C , can be thought of as an ap-

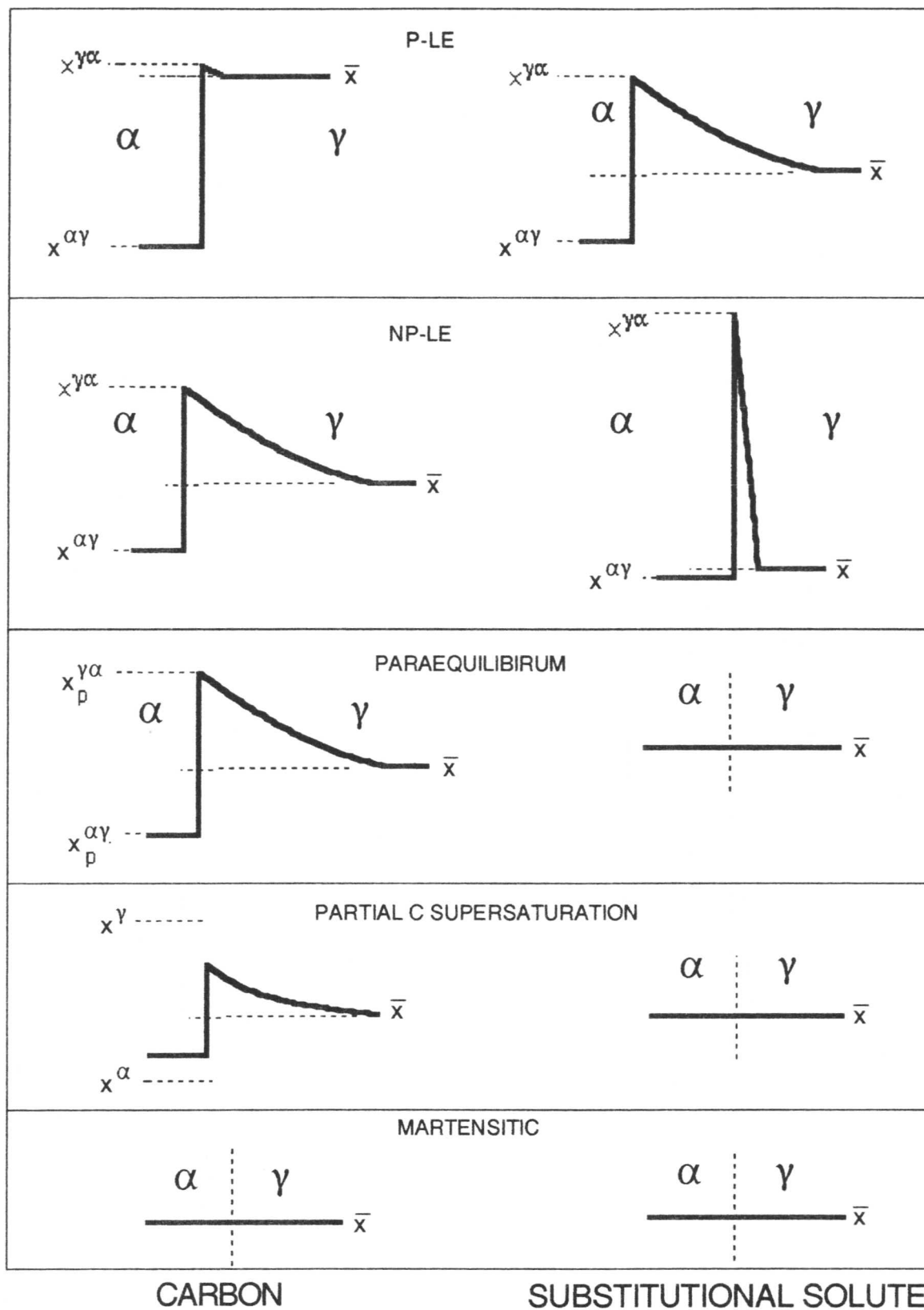
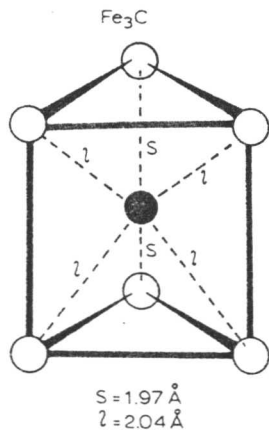


Figure 2.10: Schematic illustration of the composition variation in the vicinity of the transformation interface for a variety of growth mechanisms (Bhadeshia, 1992).

proximately hexagonal close-packed arrangement of metal atoms with localized distortions to accommodate the carbon atoms. Each carbon atom is surrounded by a triangular prism containing 6 iron atoms. This is illustrated in Figure 2.11 a). The prisms are then joined by corners and edges to form sheets stacked perpendicular to the *c*-axis, leading to the ‘pleated’ structure illustrated in Figure 2.11 b).

a)



b)

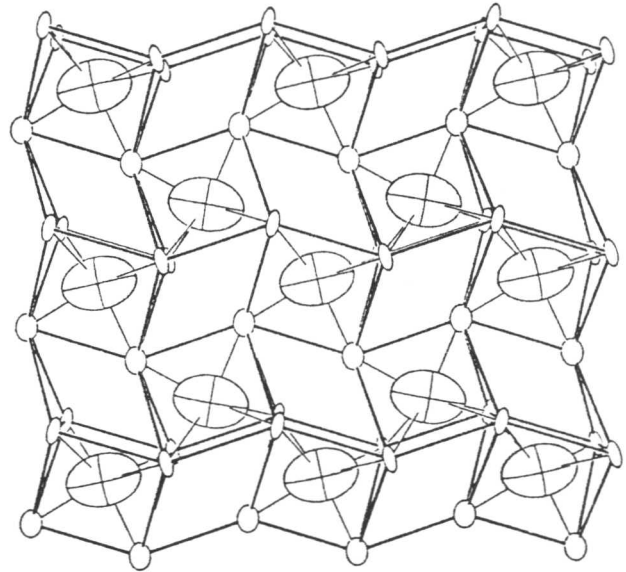


Figure 2.11: a) The triangular prism environment of iron atoms around carbon in Fe_3C (after Jack and Jack, 1973), and b) View of the atomic arrangement in cementite (after Yakel, 1985). Within each ellipse there is a 99.9% probability of finding the atom. The sizes of the ellipses depend on thermal vibration parameters, and hence the larger ellipses represent the carbon atoms.

M_3C is predominantly an iron-rich carbide with the same orthorhombic structure as Fe_3C , however several alloying elements can partition to this carbide in significant quantities. The unit cell dimensions are affected by partial substitution of alloying elements. Woodhead and Quarrell (1965) have found that Mn can dissolve in large quantities, as can Cr, with up to one fifth of the Fe atoms being replaced by Cr (specific to low alloy steels). Ni and Co can also dissolve as they form metastable orthorhombic carbides, although they usually partition to ferrite. Mo, W and V have also been found to have limited solubilities in M_3C . In general M_3C carbides can be referred to using the general formula $(\text{Fe,Cr,Mn,Mo})_3\text{C}$.

2.5.2 M_7C_3

This is a Cr-rich carbide with the trigonal structure of Cr_7C_3 , having a solubility of Fe up to 60% (although Titchmarsh (1978) has found that the Cr:Fe ratio can be greater than 1 in $2\frac{1}{4}\text{Cr1Mo}$ steel). Mn, V and Mo can also dissolve, with decreasing probabilities respectively.

Baker and Nutting (1959) state that nucleation of M_7C_3 can only occur in the vicinity of cementite or at the cementite/ferrite interface, which is supported by Kuo (1953) who states that separate nucleation is improbable because there is not enough Cr in the matrix. Beech and Warrington (1966) state that cementite particles on the point of dissolving may leave areas sufficiently rich in chromium in which M_7C_3 could precipitate since these will be the most favourable sites.

An interesting feature of M_7C_3 is that electron diffraction patterns show characteristic streaks, making it easily distinguishable from other carbides. The streaks have been attributed to faults lying on $\{10.0\}$ planes, with the fault vector being approximately half the unit cell repeat distance (Beech and Warrington, 1966).

2.5.3 $M_{23}C_6$

This is usually a Cr-rich carbide having the complex f.c.c. structure of $Cr_{23}C_6$, however, in steels containing significant amounts of Mo it can have the formula $Fe_{21}Mo_2C_6$. In steels containing both Cr and Mo its composition can be anywhere between the above. Mn has also been found to partition to $M_{23}C_6$ in small quantities. Baker and Nutting (1959) and others observe that $M_{23}C_6$ has never been found in the vicinity of M_7C_3 colonies. Beech and Warrington (1966) also support this view, finding no evidence supporting an 'in-situ' mechanism for the transformation $M_7C_3 \rightarrow M_{23}C_6$.

2.5.4 M_6C

M_6C is essentially a Mo-rich carbide with a f.c.c. structure. In a simple ternary system of Fe-Mo-C, it exists in the range Fe_2Mo_4C or Fe_3Mo_3C depending on the Mo content (Kuo, 1956). M_6C may also take small quantities of Cr and V into solution. It forms at grain boundaries, growing rapidly at the expense of all surrounding carbides, nucleating at existing particles. The transformation Mo_2C to M_6C occurs more rapidly in bainite than in ferrite.

2.5.5 M_2C

As with M_6C , M_2C is also a Mo-rich carbide with an f.c.c. structure and is usually denoted simply by Mo_2C . Cr and V have been found to be soluble in significant quantities, with a much smaller amount of Fe also dissolving. It commonly precipitates as fine needles parallel to the $\langle 110 \rangle_\alpha$ direction in ferrite. The orientation relationship is that of Pitsch-Schrader (1958):-

$$(0001)_{Mo_2C} \parallel (011)_\alpha \text{ and } [11\bar{2}0]_{Mo_2C} \parallel [100]_\alpha .$$

The precipitation of Mo_2C is usually said to be the major factor in conferring creep resistance on low alloy ferritic steels.

Table 2.1: A summary of data for the common alloy carbides found in steels, (Andrews *et al*, 1967).

Carbide	Structure	Lattice Parameter /Å	Formula Units /Cell	Density /g cm ⁻³
M ₃ C	Orthorhombic	a=4.5241 b=5.0883 c=6.7416	4	7.704
M ₇ C ₃	Trigonal	a=13.982 c=4.506	8	6.965
M ₂₃ C ₆	Cubic F	a=10.638	4	6.996
M ₆ C	Cubic F	a=11.082	16	6.325
M ₂ C	Hexagonal	a=3.002 c=4.724	1	9.188

Data for the various alloy carbides discussed above are summarised in Table 2.1.

2.6 Interphase precipitation

A number of studies (Berry and Honeycombe, 1970; Edmonds and Honeycombe, 1973; Tillman and Edmonds, 1974; Honeycombe, 1976; Dunlop and Honeycombe, 1976) have been made of the so-called *interphase precipitation* in isothermally transformed alloy steels. It was shown that direct decomposition of alloyed austenite containing a substantial amount of strong carbide-forming elements (e.g. V, Mo, Ti, Cr) can lead to a distribution of alloy carbide in the ferrite. Berry and Honeycombe (1970) investigated a number of alloys containing different amounts of Fe, Mo and C isothermally transformed in the range 600–900°C. They found two different morphologies of the carbide M₂C in the allotriomorphic ferrite; long, straight fibres growing from the prior austenite grain boundaries and sheets of smaller, needle-like, particles in a Widmanstätten ferrite array. It is these sheets of smaller particles which are termed ‘interphase precipitation’. It was found that the fibrous form of M₂C was favoured when the growth of allotriomorphic ferrite is slow, i.e. below the nose of the time-temperature transformation curve in the range 600–700°C, whereas the interphase precipitation was found at higher transformation temperatures. The orientation relationship derived between the M₂C fibres and the ferrite matrix was

$$(011)_{\alpha} \parallel (0001)_{\text{Mo}_2\text{C}}$$

$$(101)_{\alpha} \parallel (1\bar{1}01)_{\text{Mo}_2\text{C}}$$

$$[1\bar{1}1]_{\alpha} \parallel [1\bar{2}10]_{\text{Mo}_2\text{C}},$$

a relationship commonly observed for hexagonal phases precipitating within a b.c.c. matrix. The Widmanstätten ferrite type M_2C carbides were found to have the orientation relationship

$$(011)_\alpha \parallel (0001)_{M_2C}$$

$$(100)_\alpha \parallel (2\bar{1}\bar{1}0)_{M_2C}$$

$$[100]_\alpha \parallel [2\bar{1}\bar{1}0]_{M_2C},$$

which is also that describing the precipitation of M_2C in tempered martensite.

Edmonds and Honeycombe (1973) compared the microstructure and mechanical properties of a Fe-4Mo-0.2C steel both in the quenched and tempered and the isothermally transformed conditions. The isothermally transformed specimens showed elongation and high ductility when fractured, whereas the quenched and tempered specimens showed no elongation and there was evidence of cracking along the prior austenite grain boundaries. The ductile-brittle transition was found to be 30–40°C lower for the isothermally transformed alloy. These observations can be explained by the fact that the formation of alloy carbide in fibre or sheet form at the grain boundaries prevents the passage of dislocations, resulting in strong dispersion strengthening.

Honeycombe (1976) discusses the mechanism for the growth of the interphase precipitates. Early ideas for the mechanism of interphase precipitation were that the precipitates had nucleated on dislocations, known to be favourable sites for carbide nucleation. However, this would not explain the very regular precipitate arrays observed. Ferrite/austenite interfaces vary from high energy random boundaries to low energy planar boundaries which grow by step-by-step propagation. The nature of the interface itself is very important in determining the morphologies of the different carbide dispersions. The ferrite interfaces associated with interphase precipitation grow mainly by a ledge mechanism. Nucleation occurs on the planar boundary whereas the ledge itself is free from precipitates because of its higher mobility. The planar boundary is of low energy with limited mobility and therefore the growth of ferrite occurs by movement of a series of incoherent high energy steps. The fibrous carbides nucleate at the austenite boundary and then grow into the ferrite where the interface is more irregular with local curvature. Diffusivity along a disordered boundary is greater than on a coherent or semi-coherent one and therefore fibrous carbides are associated with lower temperatures and incoherent interfaces where there are enhanced diffusion paths.

CHAPTER 3

THEORETICAL STUDIES – AN INTRODUCTION

In this chapter a theoretical model for the diffusion of substitutional alloying elements to cementite particles is developed. Symmetric and asymmetric particle distributions are considered. The method of calculation of the equilibrium concentrations in the phases involved and choice of diffusion coefficients are discussed.

CHAPTER 3

THEORETICAL STUDIES – AN INTRODUCTION

3.1 Introduction

A large amount of experimental data has been collected over the years concerning the chemical composition of various carbides as a function of different tempering treatments. The aim of this work is to develop a sound theoretical basis for the assessment of these data. Carruthers and Collins (1981) and Afrouz *et al.* (1983) have attempted to explain the mechanism of composition changes in pearlitic and bainitic cementite in terms of diffusion-controlled coarsening theory (Wagner, 1961; Lifshitz and Slyozov, 1961). They therefore plotted composition changes as a function of $t^{\frac{1}{3}}$, where t is the time at the tempering temperature, and, finding approximately linear relationships, inferred that the changes occurred in the context of a coarsening reaction. However, it is well established (see for example Greenwood, 1969 and Christian, 1975) that coarsening reactions in alloys are dependent on the fact that the equilibrium composition of the matrix in contact with a particle is a function of the principal radii of curvature of the particle/matrix interface. For example, the matrix adjacent to smaller spherical particles would be expected to have a higher equilibrium concentration of solute than that adjacent to larger particles. Hence, a diffusion flux is stimulated from the smaller to the larger particles resulting in the larger particles growing at the expense of the smaller ones. The driving force for this process is the reduction in total interface energy.

However, the changes in cementite composition are fundamentally different from a coarsening reaction. The matrix is supersaturated in solute with respect to nearly all the particles and so the concentration of solute will at first increase in all particles irrespective of size. The flux of interest is that of solute into a particle from the surrounding matrix for both large and small particles. It is not correct therefore to explain the changes in particle composition in terms of coarsening theory. The enrichment behaviour only of cementite particles is discussed in this chapter. It should be noted, however, that coarsening in the true sense may occur at very long service times and also needs to be considered in the development of the model. The possibility that simultaneous coarsening and enrichment may occur is discussed in Chapter 9.

3.2 Partitioning in pearlitic and bainitic cementite

The precipitation of carbides during the bainite transformation has already been discussed in Chapter 2. After the formation of carbides, bainitic microstructures are a long way from

equilibrium. Hultgren (1947, 1951) established that upper bainitic cementite has a substitutional alloy content close to (or slightly higher than) that of the steel as a whole rather than its equilibrium concentration. Chance and Ridley (1981) investigated chromium partitioning during isothermal transformation for bainitic and pearlitic microstructures using analytical electron microscopy on carbon extraction replicas. They found that in upper bainite the partition coefficient, defined to be the ratio of chromium in cementite to that in ferrite, k_{Cr} , was close to unity. In the case of pearlitic cementite, the amount of partitioning increases with transformation temperature. At low temperatures (500–600°C) k_{Cr} remained approximately constant at $\simeq 4$, and rose to a value of $\simeq 15$ at 730°C. This is illustrated in Figure 3.1.

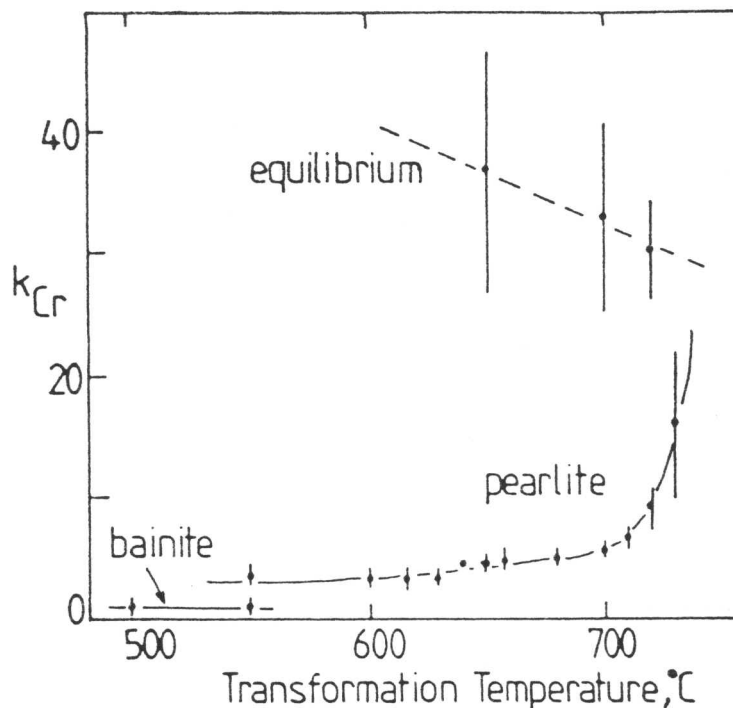


Figure 3.1: Partition coefficient between cementite and ferrite as a function of transformation temperature (Chance and Ridley, 1981).

The carbon concentration of cementite is substantially larger than that of austenite or ferrite, cementite (M_3C) containing 25 at.% of carbon to maintain the stoichiometry. A transformation to cementite, which has the same Fe/Cr ratio as the parent phase, should give a partition coefficient which is greater than unity. It can be concluded that the formation of cementite during transformation to upper bainite involves only a small degree of redistribution of elements such as chromium. This is consistent with the fact that upper bainitic cementite forms from carbon-enriched austenite, and so the driving force for cementite formation is higher allowing greater departure from the equilibrium composition.

For pearlitic cementite, however, it is found that its composition directly after transformation is always between equilibrium and paraequilibrium for alloy steels (Chance and Ridley, 1981; Al-Salman *et al.*, 1979; Williams *et al.*, 1979). Transformation to pearlite involves the co-operative growth of ferrite and cementite, with the reaction front providing a boundary along which the chromium can redistribute providing the reaction is not too rapid. There is at present no theory to predict the starting composition of pearlitic cementite from austenite, consequently modelling of the composition changes in carbides has so far focussed on bainitic cementite. If the starting composition of pearlitic cementite is known from experimental data, then the enrichment behaviour can be modelled. This is illustrated in Chapter 6.

3.3 Equilibrium compositions of cementite and ferrite

For many years the equilibrium compositions of the various carbides in alloyed steels were not known. Vengopalan and Kirkaldy (1978) determined expressions for the partition coefficient, k_z , of alloying elements between cementite and ferrite using empirical constants defined by the expression

$$k_z \approx \exp \frac{(A + BT)}{RT} , \quad (3.1)$$

for dilute alloys. The values of the constants A and B are given in Table 3.1.

Table 3.1: Parameters used for the calculation of partition coefficients (Vengopalan and Kirkaldy, 1978).

Element Z	A, J mol ⁻¹	B, J mol ⁻¹ K ⁻¹
Cr	47028	-17.45
Mn	42844	-20.21
Mo	27363	-5.86
Ni	-2619	-2.80
Si	0	-25.10

The partition coefficient k_z is defined to equal $c^{\theta\alpha}/c^{\alpha\theta}$, therefore using the condition for mass-balance at equilibrium (the Lever rule)

$$V_\theta = \frac{(\bar{c} - c^{\alpha\theta})}{(c^{\theta\alpha} - c^{\alpha\theta})} , \quad (3.2)$$

with respect to the carbon concentrations in the cementite and ferrite, $c^{\theta\alpha}$ and $c^{\alpha\theta}$, respectively the volume fraction of cementite in the alloy, V_θ , can be determined. \bar{c} is the average carbon concentration in the bulk alloy. Using the definition of the partition coefficient and the above

expression, the equilibrium compositions of the two phases can be calculated as a function of temperature using the equation:

$$c^{\theta\alpha} = \frac{\bar{c}}{V_\theta - \frac{V_\theta}{k_z} + \frac{1}{k_z}} \quad (3.3)$$

where $c^{\theta\alpha}$ and $c^{\alpha\theta}$ are now the concentrations of the substitutional alloying elements in the cementite and ferrite respectively.

However, implicit in this expression is the assumption that the solution is dilute, and it is not valid for steels with more than a few percent of the alloying elements. This method was used to find the equilibrium concentration of the various alloying elements between cementite and ferrite in the 12Cr1MoV steel discussed in Chapter 7, and was found to break down, predicting more than 100 at.% of chromium in the cementite!

It is now possible to calculate the equilibria in multicomponent alloys using experimentally determined thermodynamic data without using any dilute solution approximations and taking into account the effects of all the alloying elements in the steel. Phases other than cementite and ferrite can also be taken into account. In this work equilibrium calculations were performed using the National Physical Laboratory's Metallurgical and Thermodynamic Data Bank (MT-DATA), a computer package containing critically assessed thermodynamic data for a number of alloy systems. MTDATA allows the equilibria in multicomponent, multiphase systems to be calculated from a knowledge of the thermodynamic data for the subsystems. It is possible to calculate for a given temperature, pressure or volume, the phases present and the amounts of species within each phase by minimising the Gibbs free energy of the system for specified component amounts. Further details are given by Hodson (1989). The main database used for the calculations in this work is the solution database created by the Scientific Group Thermodata Europe.

For a specific steel composition and temperature the equilibrium phases can first be determined. The calculation yields information on the alloy content of the phases in question, their relative proportions and the Gibbs free energy of the system. If the equilibrium carbide phase is then suppressed and the calculation repeated, the new equilibria will contain the second most stable carbide. By repeating this process it is possible to predict the sequence of carbide formation on tempering steels alloyed with chromium and molybdenum. The results of specific calculations to determine the composition of the ferrite and carbide phases and precipitation sequences are presented in Chapters 5, 6 and 7 for the $2\frac{1}{4}\text{Cr}1\text{Mo}$, $\frac{1}{2}\text{Cr}\frac{1}{2}\text{Mo}\frac{1}{4}\text{V}$ and 12Cr1MoV steels respectively.

3.4 Diffusion coefficients

In a binary alloy an empirically defined diffusion coefficient is simply the proportionality constant relating the rate of transfer of diffusing substance through a unit area of section and the concentration gradient measured normal to the section. A *tracer diffusion coefficient* represents the diffusivity of radioactively labelled isotopes in an otherwise chemically homogeneous solution. When the radioactive tracer atoms are of the same species as the atoms of the medium, the tracer diffusion coefficient is called the *tracer self-diffusion coefficient*.

However, these two coefficients are not applicable if the diffusion is taking place in a concentration gradient. In the presence of a chemical composition gradient, an additional virtual force acts on the diffusing species due to the chemical potential gradient associated with the composition gradient. In order to take this into account and therefore represent the flux of one component, A, of a binary solid solution A–B in a concentration gradient of A, an *intrinsic diffusion coefficient* should be used.

In this work intrinsic chemical diffusion coefficients are used from the work of Fridberg *et al.* (1969). In order to calculate the overall diffusion coefficient, the expression

$$D = D_0 \exp\left(-\frac{Q}{RT}\right), \quad (3.4)$$

is used, where Q is the activation energy, R is the universal gas constant, T is the temperature in Kelvin and D_0 is the pre-exponential factor for diffusion. Fridberg states that the values for the self-diffusion of iron in austenite and ferromagnetic ferrite are given by

$$D_0 = 1.6 \text{ cm}^2\text{s}^{-1} \text{ and } Q = 240,000 \text{ J mol}^{-1}$$

$$D_0 = 0.5 \text{ cm}^2\text{s}^{-1} \text{ and } Q = 240,000 \text{ J mol}^{-1}$$

respectively. The intrinsic diffusion coefficients of the various alloying elements in ferrite are then determined by comparison with the self-diffusion of iron, the difference being described by a factor independent of temperature. These diffusion coefficients refer to the interdiffusion of the alloying element in a binary system, i.e. of chromium in ferrite, molybdenum in ferrite, and therefore do not strictly relate to diffusion in a multicomponent system. The values of interdiffusion coefficients used in this work are given in Table 3.2.

Table 3.2: Chemical interdiffusion coefficients (Fridberg *et al.*, 1969).

Element	$D_0/\text{m}^2\text{s}^{-1}$	$Q/\text{J mol}^{-1}$
Cr	1.5×10^{-4}	240,000
Mn	1.0×10^{-4}	240,000
Mo	1.0×10^{-4}	240,000

It is important to note that in this work it is assumed that the diffusion of the interstitial carbon is significantly faster than the diffusion of the substitutional alloying elements and that the flux of the latter will not be influenced by the former. Carbon diffusion in ferrite has been shown not to follow a simple Arrhenius-type relationship because of the possibility of carbon occupying both octahedral and tetrahedral sites in the lattice. Using the method due to McLellan *et al.* (1965) a value of $1.5 \times 10^{-11} \text{m}^2 \text{s}^{-1}$ is obtained for the diffusivity of carbon in ferrite at a temperature of 565°C . This is approximately eight orders of magnitude faster than the diffusion of chromium in ferrite. Diffusion of the alloying element only is therefore considered to be the rate-controlling step. In a more sophisticated treatment ternary diffusion, e.g. Fe-Cr-C, would need to be considered, although it should be noted that the interdiffusion coefficients allow for a flux of the alloying element within a flux of iron.

There is little information available in the literature on the diffusivity of the alloying elements in carbides. Törndahl (1968 – cited by Fridberg *et al.*, 1969) studied the rate of diffusion of manganese in cementite. His results seemed to indicate that the value of this diffusion coefficient lies between the values in ferrite and austenite. Recent work (Barnard *et al.*, 1987) using an atom probe has attempted to measure the chromium diffusivity in bainite and cementite. They found that the value in cementite was two orders of magnitude lower than corresponding measurements in ferrite. The diffusivity of chromium in ferrite measured was, however, different by an order of magnitude from that measured previously by Bowen and Leak (1970) and the value for the interdiffusion coefficient given above. The diffusion coefficient of chromium in cementite is discussed further in Chapter 8.

3.5 One dimensional modelling

A method to enable modelling of the diffusion of substitutional solute elements to cementite, for the case of a symmetric carbide distribution, was developed by Bhadeshia (1989). It is presented here in full in order that comparisons may be drawn with the improvements in the model discussed in the following sections. The problem of cementite enrichment is not easy to solve analytically because of the need to consider soft impingement[†]. The approach used in this work is to find solutions to the governing diffusion equations using numerical methods because they can easily take into account soft impingement.

3.5.1 Symmetric case – Definition of the problem

Cementite particles within a ferrite matrix are treated as a composite one dimensional

[†] Soft impingement is the overlap of the diffusion or temperature fields, or from active regions of the same particle. Hard impingement implies physical contact between the particles.

diffusion couple in which a slab of cementite, thickness x_θ , is sandwiched between two slabs of ferrite, thickness x_α , such that

$$\frac{x_\theta}{(2x_\alpha + x_\theta)} = V_\theta, \quad (3.5)$$

where V_θ is the equilibrium volume fraction of cementite in the alloy. This analysis is based on the idea that if all the cementite particles were to be massed together in a slab of width x_θ , they would occupy the same volume fraction as a number of individual carbides in a section of ferrite of length $x_\theta + 2x_\alpha$. This approximation will be a good one if the spatial distribution of plate-like carbide particles in the steel is appropriate. The thickness of the cementite is a parameter in the program chosen to represent an actual particle size in a steel at long ageing times, $\simeq 100$ nm. The equilibrium volume fraction of cementite in the alloy, V_θ , can be found by two alternative methods. Firstly, application of the Lever rule to the binary Fe–C phase diagram gives

$$V_\theta = \frac{(\bar{c} - c^{\alpha\theta})}{(c^{\theta\alpha} - c^{\alpha\theta})}, \quad (3.6)$$

where \bar{c} is the average carbon concentration in the alloy, $c^{\alpha\theta}$ and $c^{\theta\alpha}$ are the equilibrium carbon concentrations in the ferrite and cementite respectively. It is assumed that $c^{\alpha\theta} = 0$ and $c^{\theta\alpha} = 6.67$ wt.%. This method tended to overestimate V_θ by a small amount. A second, and more accurate method, is to use the volume fraction of cementite predicted by MTDATA for the ferrite/cementite equilibria. The advantage of this method is that it takes into account all the minor alloying element additions to the bulk alloy.

It is important to set the thicknesses of the ferrite and cementite to be consistent with the calculated volume fraction of cementite present at equilibrium. To this end, the size of the ferrite slice is calculated within the program for the chosen cementite particle size.

The diffusion equation must be obeyed separately in the cementite and ferrite phases:

$$\frac{\partial c^\theta}{\partial t} = D^\theta \frac{\partial^2 c^\theta}{\partial x^2} \quad (3.7)$$

$$\frac{\partial c^\alpha}{\partial t} = D^\alpha \frac{\partial^2 c^\alpha}{\partial x^2}. \quad (3.8)$$

The particle is of a fixed size and therefore the mass balance at the cementite/ferrite interface is given by

$$D^\theta \frac{\partial c^\theta}{\partial x} = D^\alpha \frac{\partial c^\alpha}{\partial x}, \quad (3.9)$$

where the gradients in this case are evaluated at the interface.

3.5.2 Symmetric case – Numerical solution

In the analysis non-dimensional variables are used. The advantage of this is that numbers occurring in the calculations cover roughly the same ranges for all calculations. Concentrations

are normalised with respect to the average concentration in the alloy and distances with respect to the thickness of the cementite, hence

$$x' = \frac{x}{x_\theta} \quad (3.10)$$

$$c' = \frac{c}{\bar{c}} \quad (3.11)$$

$$t' = \frac{Dt}{x_\theta^2}, \quad (3.12)$$

where D is the diffusion coefficient.

For the analysis the cementite and ferrite are divided up into a number of slices, n , of equal thickness, x_s such that,

$$n_\theta = \frac{x_\theta}{2x_s} \quad (3.13)$$

$$n_\alpha = \frac{x_\alpha}{x_s}. \quad (3.14)$$

This means that the x' - t' region is covered with a grid of rectangles of sides $\delta x'$ and $\delta t'$ respectively, hence the coordinates of a grid point (x', t') can be written $(i\delta x', j\delta t')$, where i and j are integers. The normalised concentration at that point (in ferrite) is denoted by $c'_{i,j}$. The use of finite-difference methods to obtain numerical solutions to the diffusion equation is discussed in detail by Crank (1975). The idea is that some, or all, of the derivatives in the diffusion equation are replaced by finite-difference approximations.

The explicit[†] finite difference approximation for diffusion in the ferrite matrix is given by

$$c'_{1,j+1} = c'_{i,j} + r(c'_{i-1,j} - 2c'_{i,j} + c'_{i+1,j}), \quad (3.15)$$

where

$$r = \frac{\delta t'}{(\delta x')^2},$$

and is taken to be 0.4. The value of r determines the accuracy of the method and also the computation time. A compromise value has been chosen by trial and error.

The finite difference method can be readily visualised using a graphical construction. If the value of r is taken to be $\frac{1}{2}$ for example, then equation 3.15 reduces to

$$c'_{1,j+1} = \frac{1}{2}(c'_{i-1,j} + c'_{i+1,j}). \quad (3.16)$$

[†] There are two methods of using finite difference approximations. Explicit formulae, as the name implies, express an unknown directly in terms of known values, whereas implicit formulae contain more than one unknown in each equation, necessitating the solution of a number of simultaneous equations. The latter method is usually considered to be more accurate but at the same time is very expensive in terms of computer time. The finite difference approximations are derived in Appendix I.

Hence, the concentration at a particular point after one time interval has passed is simply the arithmetic mean of the concentrations at the two adjacent points in the previous time interval. This is illustrated in Figure 3.2.

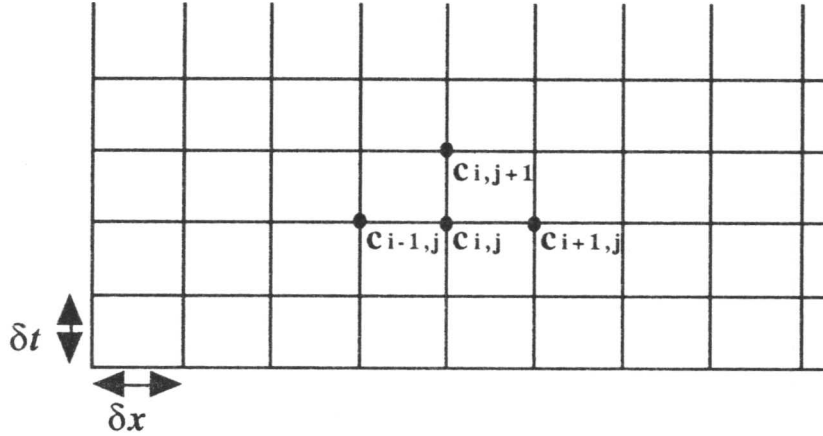


Figure 3.2: Graphical method to illustrate the finite difference model.

The normalised concentration $c_s^{\prime\alpha}$ in the α at the α/θ interface was initially set at $c^{\alpha\theta}/\bar{c}$, although the computer algorithm was designed to allow this to vary as soon as the flux matching condition at the interface necessitated changes. Then equation 3.15 was used to calculate the value of c at all points along successive time rows of the grid, for the initial conditions that $c_{0,0}^{\prime\alpha} = c^{\alpha\theta}/\bar{c}$, and $c_{i,0}^{\prime\alpha} = 1$ for all $i > 0$.

A similar analysis is applied to diffusion in the cementite. Finite difference approximations applied to the mass balance condition at the interface mean that $c_{0,j}^{\prime\theta}$ are determined by the equation

$$D_{\theta}(c_{0,j}^{\prime\theta} - c_{1,j}^{\prime\theta}) = D_{\alpha}(c_{1,j}^{\prime\alpha} - c_{0,j}^{\prime\alpha}), \quad (3.17)$$

where $c_{i,0}^{\prime\theta} = 1$ for all $i > 0$. It should be noted that the value of the concentration in cementite at the interface was not fixed by local equilibrium considerations, but increased gradually with time towards the equilibrium level. It is assumed that the diffusion coefficients in cementite and ferrite are equal for this work. This is discussed further in Chapter 8. In general $c^{\theta\alpha} \gg c^{\alpha\theta}$, therefore this condition ensures that the surface concentration of cementite at the θ/α interface, $c_{0,j}^{\prime\theta}$, is for a considerable period of time, less than $c^{\theta\alpha}/\bar{c}$.

For both phases, soft impingement will eventually occur. This means that the concentrations at the maximum values of i for both θ and α are eventually affected by the fluxes originating at the θ/α interface. The concentrations in the slices with $i = i_{max}$ (i.e. the extent of the ferrite and at the centre of the cementite particle) are therefore given by reflecting the concentration profile across an imaginary boundary located at i_{max} , hence

$$c_{i_{max},j+1}^{\theta} = c_{i_{max},j}^{\theta} + 2r(c_{i_{max}-1,j}^{\theta} - c_{i_{max},j}^{\theta}). \quad (3.18)$$

The diffusion couple and notation used are illustrated in Figure 3.3.

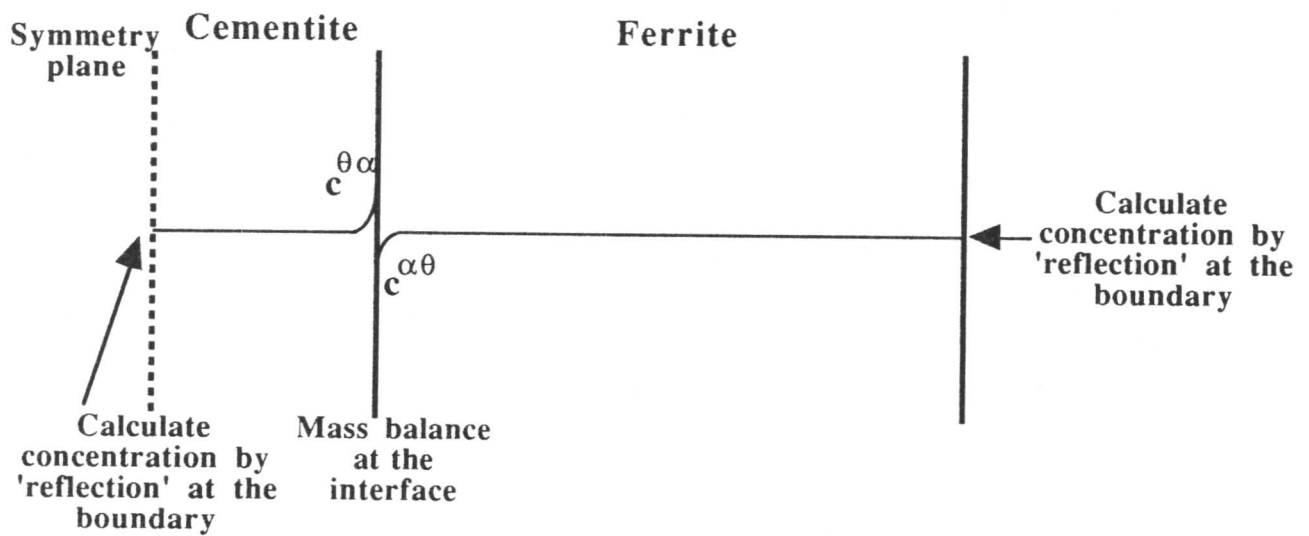


Figure 3.3: The diffusion couple and notation used for calculation of the enrichment rate of cementite in the symmetric case.

As the diffusion proceeds, $c_{0,j}^{\theta}$ eventually reaches $c^{\theta\alpha}/\bar{c}$ (at very long times). When this has occurred, it is diffusion in the cementite which begins to control the equilibration process, and the program switches to adjusting $c_{0,j}^{\alpha}$ to a value consistent with the condition for conservation of mass at the interface. The value of $c_{0,j}^{\alpha}$ then begins to increase to a value greater than $c^{\alpha\theta}/\bar{c}$.

It has already been stated that the diffusion coefficients of substitutional alloying elements in cementite are not known accurately. The sensitivity of the computer model to the value of the diffusion coefficient of Cr in cementite, D_{θ} , has been investigated. As the magnitude of the diffusion coefficient in cementite is reduced there are two main effects. The first is that the concentration in cementite at the particle/matrix interface rises more quickly as D_{θ} becomes

lower than D_α because of the need to satisfy the condition for mass balance at the interface (Equation 3.17). The second effect is an increase in the concentration gradient within the cementite particle because more time is necessary to redistribute the alloying element from the interface. For smaller particles, this will result in the overall enrichment rate being quicker because, although the diffusion coefficient is smaller, the diffusion distance is still comparable to the particle size and the increased concentration at the interface is able to redistribute across the particle. Larger particles, for which the diffusion distance is smaller than the size of the particle, are not affected significantly. (The diffusion distance, x , of a given element in a specific length of time, t , can be estimated using the formula $x^2 = Dt$ where D is an appropriate diffusion coefficient.)

Low-alloy steels used in the power generation industry, having been continuously cooled from the austenising temperature, are usually given a high temperature ($\simeq 700^\circ\text{C}$) stress-relief heat treatment before entering service at the lower temperature of $\simeq 565^\circ\text{C}$. Consequently, two computer programs have been developed, the first one (FINITE) is used for modelling the changes which take place during the stress-relief heat treatment, and the second (FINN), for which the input is the data generated by FINITE, to simulate the composition changes which occur during service after the stress-relief heat treatment. The computer program FINITE is presented in Appendix II.

The effect of temperature on the enrichment rate is illustrated in Chapter 5, the temperature dependence coming from the temperature dependence of the diffusion coefficient (equation 3.4) and the temperature variation of the equilibrium calculated level of substitutional alloying elements in cementite. Calculations are performed for a cementite particle in a $2\frac{1}{4}\text{Cr}1\text{Mo}$ steel, with a size of 60 nm at temperatures of 510, 565 and 620°C . The effect of particle size on the enrichment rate is discussed in Chapters 5 and 6 for $2\frac{1}{4}\text{Cr}1\text{Mo}$ and $\frac{1}{2}\text{Cr}\frac{1}{2}\text{Mo}\frac{1}{4}\text{V}$ steels respectively.

3.5.3 Asymmetric case – Definition of the problem

For the case in which the amount of ferrite on either side of the carbide plate is different, the central plane of the carbide is no longer a mirror plane and it becomes necessary to consider an asymmetric carbide distribution. The method of solution of the diffusion equations for an asymmetric carbide distribution is essentially the same as that for the symmetric case. Only the significant differences are highlighted below. The problem is initially set up with a slice of cementite of thickness x_θ in between two slices of ferrite (identified by the labels a and b) of

different thicknesses, $x_{\alpha a}$ and $x_{\alpha b}$ such that

$$\frac{x_{\theta}}{(x_{\alpha a} + x_{\theta b} + x_{\alpha b})} = V_{\theta}. \quad (3.19)$$

The input parameters for the calculation are the chosen particle size and volume fraction and a constant which represents the degree of inhomogeneity in the microstructure, the ratio of the thickness of ferrite (a) to ferrite (b). Hence, the program automatically calculates the thickness of the two ferrite slices to be consistent with the desired volume fraction and distribution of carbide.

The diffusion equation must be satisfied independently in both slices of ferrite and the cementite:

$$\frac{\partial c^{\theta}}{\partial t} = D^{\theta} \frac{\partial^2 c^{\theta}}{\partial x^2}, \quad (3.20)$$

$$\frac{\partial c^{\alpha a}}{\partial t} = D^{\alpha} \frac{\partial^2 c^{\alpha a}}{\partial x^2}, \quad (3.21)$$

$$\frac{\partial c^{\alpha b}}{\partial t} = D^{\alpha} \frac{\partial^2 c^{\alpha b}}{\partial x^2}. \quad (3.22)$$

3.5.4 Asymmetric case – Numerical solution

The number of slices in the cementite and ferrite are given by

$$n_{\theta} = \frac{x_{\theta}}{2x_s}, \quad (3.23)$$

$$n_{\alpha a} = \frac{x_{\alpha a}}{x_s}, \quad (3.24)$$

$$n_{\alpha b} = \frac{x_{\alpha b}}{x_s}. \quad (3.25)$$

The finite difference approximations to the diffusion equation are the same as in the symmetric case (equation 3.15) with an additional equation being added for the second ferrite slice. The boundary conditions are the same as for the symmetric case, although in the asymmetric case there are four, rather than two, boundaries to be considered. Soft impingement is taken into account at the extremes of the two ferrite slices in the same manner as equation 3.18. This allows the different fluxes originating from the two ferrite/cementite interfaces to be taken into account. The condition for mass balance (equation 3.17) is applied separately at the interfaces between cementite and ferrite (a), and between cementite and ferrite (b). Both $c^{\alpha\theta a}$ and $c^{\alpha\theta b}$ are initially set to $c^{\alpha\theta}/\bar{c}$, but are then allowed to vary independently because of the asymmetric carbide distribution. The numerical calculation of the level of substitutional solute in the cementite takes into account the differences in the interface values. The asymmetric diffusion

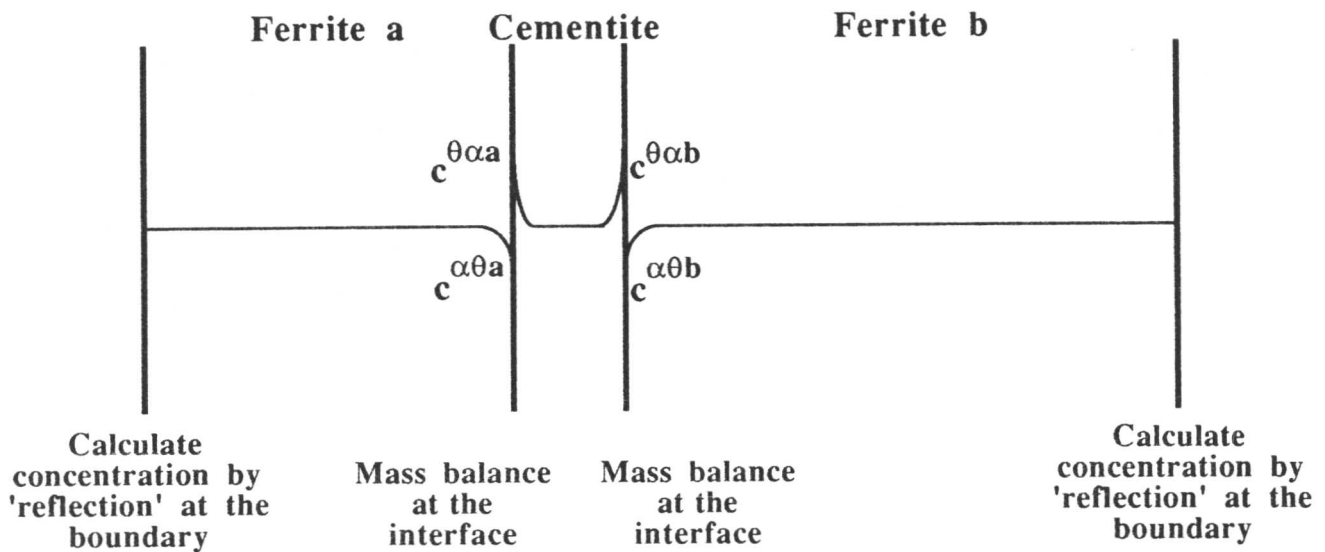


Figure 3.4: The diffusion couple and notation used for calculation of the enrichment rate of cementite in the asymmetric case.

couple and the notation used in the calculation of enrichment rate are illustrated in Figure 3.4. The computer program used in the asymmetric case (INHOMOG) is presented in Appendix III.

Figure 3.5 illustrates the effect of varying degrees of inhomogeneity in the microstructure. The chromium content of a cementite particle of size 60 nm is plotted as a function of the square root of time for a symmetric distribution, and for one ferrite slice being twice and five times as big as the other. The calculations were done at a temperature of 565°C for a $2\frac{1}{4}\text{Cr1Mo}$ steel. It can be seen that there is a marked reduction in the enrichment rate as the microstructure becomes more inhomogeneous. This is due to soft impingement in the smaller ferrite slice happening earlier than in the symmetric case and slowing down the rate of diffusion.

Figure 3.6 shows the actual chromium concentration profiles through the diffusion couple, one ferrite slice being twice the size of the other. The cementite particle size was chosen to be 50 nm and the calculations were again performed at 565°C for a $2\frac{1}{4}\text{Cr1Mo}$ steel. Four curves are shown on the graph representing intermediate times of 40, 100, 200 and 3,500 hours in the diffusion process. The average chromium concentration in the cementite particle can be seen to be gradually increasing as a function of time as it approaches equilibrium. After 3,500 hours the profiles are flat in both the cementite and ferrite, indicating that saturation has been reached.

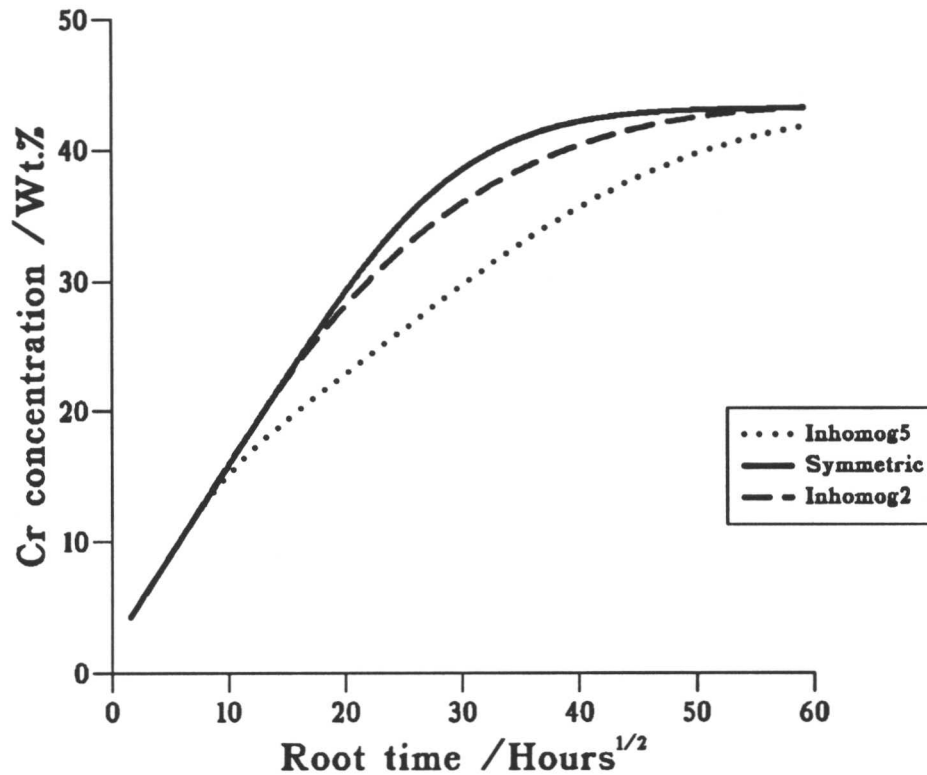


Figure 3.5: Chromium concentration in a cementite particle as a function of the square root of time for varying degrees of inhomogeneity in the microstructure.

Soft impingement can also be seen to be occurring more rapidly in the shorter ferrite slice; the concentration at the extent of the ferrite drops as it begins to be affected by fluxes originating at the interface.

The chromium profile inside the cementite particle used in Figure 3.6 is illustrated in Figure 3.7. The profile corresponds to a diffusion time of 100 hours. The slightly asymmetric profile in the cementite particle reflects the fact that soft impingement has occurred in the smaller ferrite slice. Comparison of the prediction of the asymmetric model with experimental results are made in Chapter 5.

3.6 Consideration of the effect of particle size

The use of the finite-difference model has highlighted the strong effect of particle thickness on its average composition during ageing. For a given flux across the θ/α interface, smaller particles will be sinks for solute and will enrich at a higher rate. Output from the model has indicated that the time t_c to reach a given composition varies as $(x_\theta)^2$, although this is only the case if soft impingement has not occurred in the ferrite (corresponding to approximately 8,000 hours of service life). It is possible to account for this analytically; however, the analysis

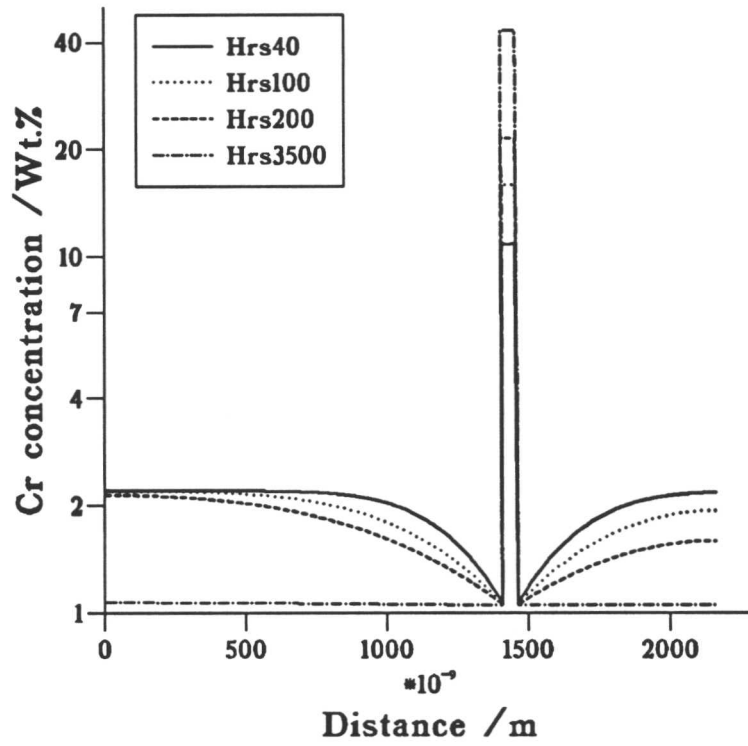


Figure 3.6: Chromium concentration profiles through a diffusion couple at times of 40, 100, 200 and 3500 hours during the diffusion process. The cementite particle size is 50 nm and the temperature 565°C.

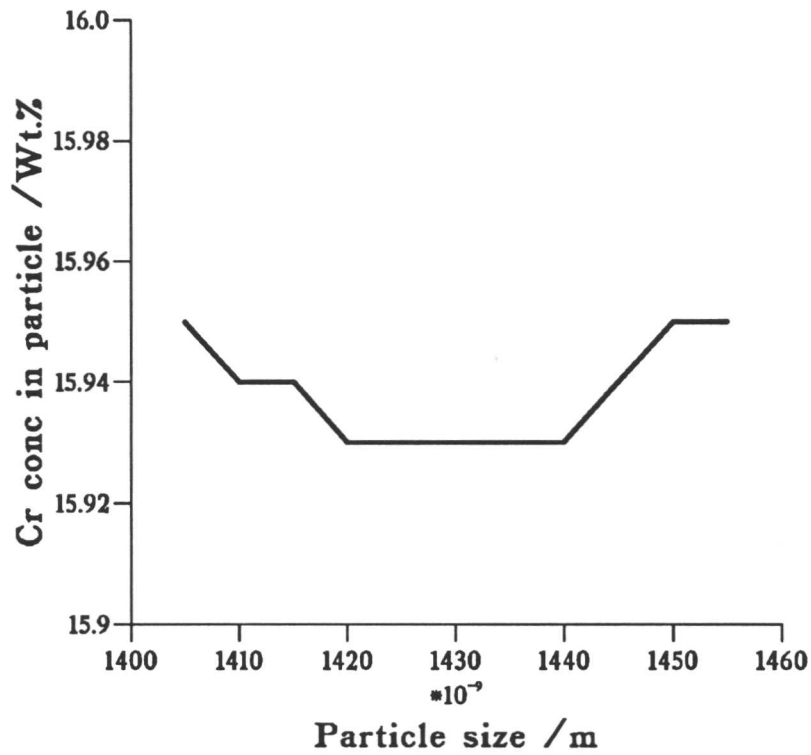


Figure 3.7: Schematic illustration of the chromium concentration profile within a cementite particle after 100 hours at 565°C.

cannot allow for the coupling of fluxes between the cementite and ferrite and so will tend to overestimate the time required to reach a given concentration.

Consider a slab of thickness x_θ embedded in an infinite matrix of ferrite (and no soft impingement in the ferrite). If the time required for the cementite to reach a concentration c^θ is t_c , then a standard mass balance procedure can be used (e.g. Crank, 1975) to show that

$$0.5x_\theta(c^\theta - \bar{c}) = \int_0^\infty c^\alpha(x, t_c) dx, \quad (3.26)$$

where

$$c^\alpha(x, t_c) = (\bar{c} - c^{\alpha\theta}) \operatorname{erfc} \left(\frac{x}{2\sqrt{D_\alpha t_c}} \right). \quad (3.27)$$

This equation can be solved to show that

$$t_c = \frac{\pi x_\theta^2 (\bar{c} - c^\theta)^2}{16D_\alpha (c^{\alpha\theta} - \bar{c})^2}. \quad (3.28)$$

It can be seen that, within the validity of the equation, the composition of cementite should vary with $t^{\frac{1}{2}}$ rather than with $t^{\frac{1}{3}}$. It should also be noted that, since $c^{\alpha\theta}$ is a relatively weak function of temperature, most of the temperature dependence of the ageing process comes from D_α . This means that for experiments carried out at various temperatures a plot of $\ln t_c$ against $1/T$ should give a positive slope corresponding to the activation energy for diffusion divided by the universal gas constant.

A similar analysis can be carried out for spherical particles, following Crank (1975). If the particle radius is a and the distance ahead of the particle is noted by r , then the solute distribution ahead of the particle is given by

$$c^\alpha(s, t_c) = \left[\frac{a(\bar{c} - c^{\alpha\theta})}{(a + s)} \right] \operatorname{erfc} \left(\frac{x}{2\sqrt{D_\alpha t_c}} \right). \quad (3.29)$$

Using the same procedure as above, it can be shown that

$$\frac{a^2(c^{\theta\alpha} - \bar{c})}{3(\bar{c} - c^{\alpha\theta})} = D_\alpha t_c + 2a\sqrt{\frac{D_\alpha t_c}{\pi}}. \quad (3.30)$$

In this case an initial enrichment proportional to $t^{\frac{1}{2}}$ is indicated, with a subsequent reduction in the time exponent. In both cases the enrichment also varies with the square of the particle radius in agreement with the numerical model. However, it is more difficult to interpret an activation energy for the spherical particles as the equation is no longer linear in D_α .

CHAPTER 4

EXPERIMENTAL PROCEDURE

The various techniques employed in the experimental studies of precipitation characteristics in $2\frac{1}{4}\text{Cr1Mo}$, $\frac{1}{2}\text{Cr}\frac{1}{2}\text{Mo}\frac{1}{4}\text{V}$ and 12Cr1MoV steels are described in this chapter.

CHAPTER 4

EXPERIMENTAL PROCEDURE

4.1 Introduction

This chapter includes a description of the experimental programme and the techniques employed, as summarised in Figure 4.1.

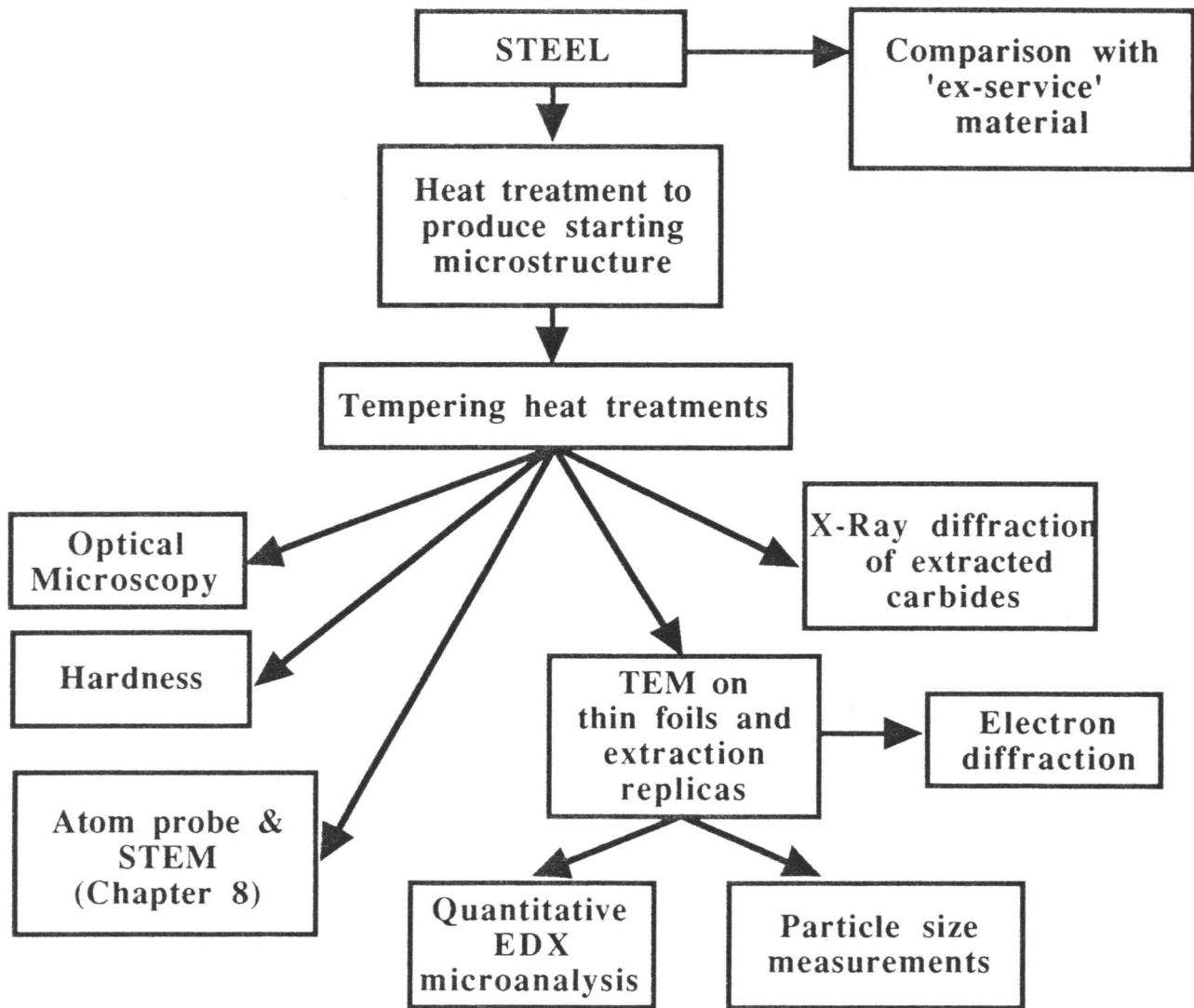


Figure 4.1: Flow chart illustrating the detailed experimental programme for three steels with different chromium contents.

4.2 Materials

The precipitation of cementite and other alloy carbide phases was examined for three typical power plant steels of varying chromium concentrations. The first was a $\frac{1}{2}\text{Cr}\frac{1}{2}\text{Mo}\frac{1}{4}\text{V}$ steel with a pearlitic microstructure which was expected to contain cementite as the dominant carbide phase at the temperatures of interest for several hundred years. The second contained slightly more chromium, $2\frac{1}{4}\text{Cr}1\text{Mo}$, the starting microstructure consisting of a mixture of bainite and martensite. Alloy carbides began to precipitate at the expense of cementite after a few hundred hours in this steel. The third steel was heavily alloyed with chromium, $12\text{Cr}1\text{MoV}$, resulting in the equilibrium alloy carbide precipitating within a few minutes on tempering at elevated temperatures. The chemical compositions of the steels used are given in Table 4.1. Further details of the materials supplied and heat treatments employed are given in Chapters 5, 6 and 7 for the $2\frac{1}{4}\text{Cr}1\text{Mo}$, $\frac{1}{2}\text{Cr}\frac{1}{2}\text{Mo}\frac{1}{4}\text{V}$ and $12\text{Cr}1\text{MoV}$ steels respectively. The $\frac{1}{2}\text{Cr}\frac{1}{2}\text{Mo}\frac{1}{4}\text{V}$ steel was supplied as prepared carbon extraction replicas from previous work by Du (1986). Details of the original method of preparation of the replicas are included below for completeness. Additional measurements were made on these specimens in order to relate particle size and chemical composition.

Table 4.1: Chemical composition of the steels used in wt. %

Steel	C	Si	Mn	P	S	Cr	Mo	V	Ni	Cu	Co	Nb+Ta	As	Sn
$\frac{1}{2}\text{Cr}\frac{1}{2}\text{Mo}\frac{1}{4}\text{V}$	0.14	0.23	0.61	0.007	0.023	0.36	0.66	0.26	0.21	0.13	–	–	–	–
$2\frac{1}{4}\text{Cr}1\text{Mo}$	0.15	0.29	0.49	0.01	0.025	2.20	0.96	0.01	0.14	0.18	0.02	–	0.03	0.02
$12\text{Cr}1\text{MoV}$	0.21	0.25	0.46	0.009	0.012	10.9	1.03	0.30	0.52	0.02	0.02	0.06	–	–
Ex-service 'X20CrMoV12'	0.18	0.22	0.58	0.01	0.007	12.4	1.07	0.28	0.64	0.13	0.03	<0.01	–	–

4.3 Heat treatments

4.3.1 Furnace heat treatments

Prior to the tempering heat treatments, the samples were sealed in silica tubes under a partial pressure of argon (150 mm Hg) to prevent any decarburisation or oxidation. The quartz tubes were then placed on ceramic boats inside furnaces to prevent any contamination by contact with the base of the furnace. The furnace temperatures were checked at regular intervals during the long term heat treatments with a Pt/Pt–13 wt.% Rh thermocouple.

4.3.2 Thermomechanical simulator heat treatments

A thermomechanical simulator ('Thermecmastor' manufactured by Fuji Electronic Industrial Co. Ltd.) was used in order to control and follow the initial heat treatments of the $2\frac{1}{4}\text{Cr1Mo}$ steel more accurately than could be achieved in a furnace. The Thermecmastor incorporates a sophisticated dilatometer, although is usually used for investigations of the effects of stress on transformation because the strains can be monitored in two orthogonal directions. It has a high frequency induction heating system, allowing homogeneous heating of the specimen to within $\pm 5^\circ\text{C}$, and is computer controlled enabling the heat treatment cycle to be programmed and monitored with ease. Heating can be done under a vacuum or with a gas atmosphere (Ar, N_2). Rapid heating and cooling at specified rates are also possible, with the gases Ar, He or N_2 being used for quenching. In this work heating was performed in an argon atmosphere and quenching was done with nitrogen gas. Temperature is measured using a Pt/Pt-13 wt.% Rh thermocouple resistance welded to the specimen. The dilation of the specimen in a radial direction during transformation is measured using a laser beam. Specimens for tests (under compression or with no applied load) are cylinders of 8 mm diameter and 12 mm long.

In order to prevent surface oxidation and nucleation effects (Strangwood and Bhadeshia, 1987), the specimens were nickel plated before use in the Thermecmastor. The nickel plating was carried out in two stages. Firstly, an adherent but rough layer of Ni was plated onto the surface by a 'striking' treatment in a solution of 250 g of nickel sulphate, 27 ml of concentrated sulphuric acid and 1 litre of water, with an applied current density of 7.75 mA mm^{-2} , for 6 minutes. After striking the samples were plated in a solution containing 140 g nickel sulphate, 140 g anhydrous sodium sulphate, 15 g of ammonium chloride and 20 g boric acid made up to a litre with distilled water. The applied current density was 0.4 mA mm^{-2} , and plating was carried out for 30 mins resulting in a nickel layer thickness of approximately 0.1 mm.

4.4 Hardness measurements

Macrohardness measurements were made using a Vickers pyramid hardness testing machine using a load of 30 kg and an $\frac{2}{3}''$ objective. Five measurements were taken over the whole sample area. Microhardness measurements were made with a Leitz miniload machine using a load of 0.981 N, and loading and dwell times of 15 seconds each. Twenty measurements were taken over the whole area of the specimen and the mean value calculated.

4.5 Optical microscopy

Samples were prepared for microstructural characterisation by hot mounting in acrylic moulding powder, followed by grinding on SiC paper to 1200 grit and polishing with $1 \mu\text{m}$ cloth

coated with diamond paste. Specimens of $2\frac{1}{4}\text{Cr1Mo}$ steel were etched in 2% nital (nitric acid in methanol) and specimens of the 12Cr1MoV steel were etched using Bain–Vilella's reagent (5 ml hydrochloric acid, 1 g picric acid in 100 ml of methanol) for times of up to 3 minutes. Samples of the $\frac{1}{2}\text{Cr}\frac{1}{2}\text{Mo}\frac{1}{4}\text{V}$ steel were received already in the form of carbon extraction replicas; however, these were originally etched in 4% nital for cementite extraction from the shorter time heat treatments, and in Vilella's reagent for extraction of the larger alloy carbides from the longer term heat treatments. Optical micrographs were taken with an Olympus microscope with a camera attached using Ilford Pan F film.

4.6 Transmission electron microscopy

Specimens for transmission electron microscopy (TEM) were prepared by both by the twin–jet electropolishing of thin foils and the carbon extraction replica technique.

4.6.1 Thin foil preparation

Thin 3 mm discs are required as the starting point for thin foil preparation. These were cut directly from the heat–treated 3 mm rods of the 12Cr1MoV steel using a SiC slitting wheel, whereas 3 mm discs were mechanically punched out of thin slices cut from the larger rectangular specimens of $2\frac{1}{4}\text{Cr1Mo}$ steel using a high–speed saw. The discs were then mechanically ground by hand to 50 μm and then twin–jet electropolished to electron transparency at 50 V, with the solution being cooled to 0°C using liquid nitrogen. The polishing solution used for the 12Cr1MoV steel contained 10% perchloric acid, 15% glycerol and 75% industrial methylated spirits, and that for the $2\frac{1}{4}\text{Cr1Mo}$ steel, 5% perchloric acid, 20% glycerol and 75% industrial methylated spirits. The thinned samples were examined in a Phillips 400T TEM operated at 120 kV.

4.6.2 Extraction replica preparation

The extraction replica technique is very useful for the identification or counting of carbide or precipitate phases in a metallic system. The main advantages of replicas over foils are that they eliminate any effects due to the steel matrix and thus enable the chemical composition of the carbides to be measured more accurately, and working with a magnetic specimen in the electron microscope is avoided. The replica is also very thin $\simeq 100 \text{ \AA}$, has no self–structure and will not burn in an electron beam.

Single–stage carbon extraction replicas were prepared using the method described by Smith and Nutting (1956) from surfaces prepared as for optical microscopy using a lighter etch. Shadowing of the carbon replica with gold (Mukherjee *et al.*, 1968) was not considered necessary

because only the particle sizes were measured, rather than volume fractions. The presence of gold on the replica would also have interfered with the electron diffraction and quantitative EDX measurements used to identify the second phase particles. A carbon coating of 200-300 Å (colour blue-brown) was deposited in a vacuum of 10^{-5} torr on to the etched specimens. The carbon film was scored using a sharp blade to enable removal of several small sections covering the whole area of the sample. The film was then removed by electrolytic etching in a solution containing 5% hydrochloric acid in methanol at +1.5 V. The film was then washed in industrial methylated spirits and floated off in distilled water and collected on 400 square mesh copper grids for examination in the TEM. Replicas from the $\frac{1}{2}\text{Cr}\frac{1}{2}\text{Mo}\frac{1}{4}\text{V}$ steel specimens were originally prepared using 4% nital for specimens previously etched in 4% nital, and 10% nital for those previously etched in Vilella's reagent.

4.6.3 Calibration of the camera constant

The settings of the various magnetic lenses within the column of a TEM affect the magnification of diffraction patterns. Usually the microscope is operated with the lenses at fixed settings and so the magnification of the diffraction pattern is a constant. This magnification factor is expressed in terms of an equivalent camera length necessary to produce the same magnification in a diffraction camera without the lenses. This is illustrated schematically in Figure 4.2.

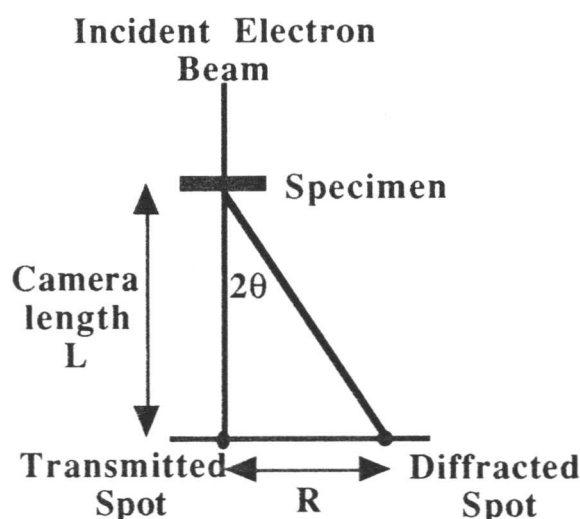


Figure 4.2: Schematic illustration of the magnification of a diffraction pattern by the microscope lenses.

The camera constant is denoted by the expression, corrected for relativistic effects,

$$Rd_{\{hkl\}} = L\lambda = \text{camera constant} \quad (4.1)$$

where R is the real distance measured on the diffraction pattern between the transmitted and the diffracted spot, L is the camera length (usually 575 mm or 800 mm in the Philips 400T TEM operated at 120 kV), $d_{\{hkl\}}$ is the spacing of the $\{hkl\}$ crystallographic planes and λ is the electron wavelength. λ is given by the following expression which is corrected for relativistic effects:-

$$\lambda = \frac{h}{2meV \left(1 + \frac{eV}{2mc^2}\right)} = 0.03335\text{\AA}, \quad (4.2)$$

where h is Planck's constant, m and e are the electron mass and charge respectively, V is the accelerating voltage of the electrons and c is the speed of light in vacuum.

It was very important for the identification of the various carbide phases which have similar lattice parameters to determine the camera constant accurately. This was done by examination of the diffraction pattern from a gold film sputtered onto a copper grid. A film produced by chemical vapour deposition consists of very fine grain size polycrystals. For a given electron beam direction a number of particles are oriented so as to satisfy the Bragg equation hence each plane gives rise to a number of reflections lying in a cone of angle 4θ . The resulting diffraction pattern therefore consists of a set of concentric rings corresponding to the $\{hkl\}$ planes which are diffracting.

To calculate the camera constant the diameters of the rings in the diffraction pattern were first measured. Then the ratios of the squares of the radii of the outer rings to those of the first or second low-index ring were determined. This enabled the N values corresponding to each of the rings to be found; N is given by the usual expression for cubic systems

$$N^2 = h^2 + k^2 + l^2, \quad (4.3)$$

where $\{hkl\}$ are the plane indices. The N values were then converted to d spacings using the formula

$$d = \frac{a}{\sqrt{N}} \quad (4.4)$$

for cubic systems. The accurate lattice parameter, a , for gold has been measured as 4.0780Å (Barrett and Massalski, 1968). Multiplication of the calculated d spacings by the radius of each individual ring gives a constant value. The average of all the values for the individual rings was used for the best accuracy. This method is illustrated in Table 4.2, which evaluates the camera constant for a current of 6.40 A through the objective lens at the eucentric specimen height. The diffraction pattern from the sputtered gold film is illustrated in

Figure 4.3. The calculated camera constants for a number of different nominal camera lengths and currents through the objective lens used in the characterisation of second phases are given in Table 4.3. The various carbides were identified using both selected area electron diffraction and convergent beam electron diffraction when the carbides were very small compared with the size of the selected area diffraction aperture.

Table 4.3: Calculated camera constants for a number of different nominal camera lengths and currents through the objective lens.

Nominal camera length /mm	Objective lens current /A	Calculated camera constant / $\times 10^{12}\text{m}^2$
800	6.40	2.66
800	6.20	2.71
575	6.20	1.86

4.7 Energy dispersive X-ray analysis (EDX)

For the detailed experimental results of particle size and composition on the $\frac{1}{2}\text{Cr}\frac{1}{2}\text{Mo}\frac{1}{4}\text{V}$, $2\frac{1}{4}\text{Cr1Mo}$ and 12Cr1MoV steels, detailed microanalyses were carried out on particles using carbon extraction replicas. At least 30 isolated particles on each specimen were analysed, depending on the particular measured composition variation, covering an area of several grid squares. In the early stages of tempering the cementite composition was found to vary so greatly between different particles that up to 100 analyses were needed to get a good estimation of the variation and a reasonable estimate of the average concentration. A LINK series 860 energy dispersive X-ray spectrometer attached to a Phillips 400T 120 kV TEM was used for all the analyses. X-ray spectra were recorded at a specimen tilt of 35° , and live times of at least 200 seconds were used to ensure statistically significant results, depending on the count rate from individual particles. The dead time was not allowed to exceed 25%. The data were analysed using the LINK RTS2-FLS software.

The original measurements on the $\frac{1}{2}\text{Cr}\frac{1}{2}\text{Mo}\frac{1}{4}\text{V}$ specimens made by Du (1986) were on extraction replicas in both a 100kV Philips 400T and a 200kV Hitachi H-700T transmission electron microscope, each equipped with an EDAX 9100 energy dispersive X-ray analysis facility. 50,000, 25,000 and 25,000 counts were preset in the Fe K_α , Mo K_α and V K_α windows respectively to keep a constant statistical error. Counts from the carbon replica background were kept at 200 ± 50 counts per second in the Hitachi H-700T and 100 ± 50 cpts in the Philips

400T microscopes to ensure a constant intensity beam. The incident spot size was 1000 Å and all the analyses were done with the spot covering the whole particle.

Chromium is chosen as an indicator of composition change because of its large concentration and partition coefficient; the iron content simply mirrors the changes in chromium content. The total manganese content is relatively small and therefore any errors will be relatively large. Molybdenum has a much larger atomic mass compared with iron, chromium or manganese. Since the microanalytic measurements are carried out assuming that all elements absorb the X-rays to a similar degree, the molybdenum data are likely to be flawed, the extent of the error depending on the thickness of the particle along the electron beam direction (a parameter which is very difficult to determine for each individual particle).

Typical EDX spectra for the various carbides in the three steels are presented in detail in the experimental chapters 5, 6 and 7.

4.7.1 Basis for quantification of EDX

Quantitative microanalysis involves the comparison of the intensities of an unknown peak with that from a measured or calculated standard, removal of the background, peak integration and correction for peak overlap. The intensity of a peak is proportional to the composition of the material being analysed. In order to avoid determination of various constants depending on mass, specimen thickness and diffraction conditions, ratios of the integrated characteristic intensities are related to the composition of the specimen using the equation due to Goldstein *et al.* (1986) for a binary system

$$\frac{C_A}{C_B} = k_{AB} \frac{I_A}{I_B}, \quad (4.5)$$

where C_A and C_B are the weight fractions of elements A and B in the analysed volume, I_A and I_B are the characteristic intensities of elements A and B (after subtraction of the background), and k_{AB} is an experimental constant. The number of similar equations for all the elements being analysed is necessarily less than the number of elements, therefore in order to solve these equations it is assumed that all the elements are detected and that the sum of the concentrations is 100%. It should be noted that due to the presence of a beryllium window on the front of the EDX detector, the carbon content of carbides cannot be allowed for. The results of the EDX analyses can be normalised to allow for the appropriate stoichiometric carbon content in the various carbides.

The factors k_{AB} , k_{AC} , k_{CB} etc. can be determined experimentally using pure elements or homogeneous compounds containing the desired element and the element chosen as a standard (Si in this case), e.g. chromium silicide, or by calculation from first principles. Experimental

determination is better due to difficulties into taking account of the detector response and other minor factors. The peak intensities and shapes from the standard compounds are used to determine the k-factors for every element to be analysed normalised with respect to Si. Pure compounds containing Si were used to determine the k-factors experimentally for the elements of interest when the EDX system was set up. The overall intrinsic system error is $\simeq 0.5\text{--}1.0\%$. The characteristic energies for the X-ray peaks of interest and the k-factors with respect to Si are given in Table 4.4.

Table 4.4: Characteristic X-ray peak energies for EDX. The average energy is given for the $K\alpha_1$ and $K\alpha_2$ peaks because, unlike X-ray diffraction, EDX is not usually able to resolve these peaks. The k-factors determined from standard compounds are included for the more intense α peaks only.

Element	Peak	Energy /keV	k_{Si}
Mo	$L_{\alpha_{1,2}}$	2.293	1.766
Mo	L_{β_1}	2.394	–
V	$K_{\alpha_{1,2}}$	4.948	1.197
Cr	$K_{\alpha_{1,2}}$	5.410	1.213
V	L_{β_1}	5.427	–
Mn	$K_{\alpha_{1,2}}$	5.898	1.291
Cr	K_{β_1}	5.946	–
Fe	$K_{\alpha_{1,2}}$	6.397	1.322
Mn	K_{β_1}	6.490	–
Fe	K_{β_1}	7.057	–
Cu	$K_{\alpha_{1,2}}$	8.037	1.595
Cu	K_{β_1}	8.940	–
Mo	$K_{\alpha_{1,2}}$	17.426	4.830
Mo	K_{β_1}	19.786	–

Correction for the absorption of characteristic X-rays in the particle analysed have been ignored, being close to unity for the average size of carbide present (< 100 nm). Characteristic X-ray fluorescence is of second order in magnitude to absorption and is therefore also ignored.

4.8 Particle size measurements

The size of each carbide particle was determined by measuring a number of random intercepts across it on the photographic negative. Hence, particle size is expressed in terms of a

mean linear intercept. This measure was chosen as it is closely related to the diffusion distance across the particle and can be used for irregular geometries. The particles are in the form of thin plates, so that most of the enrichment should be from diffusion in a direction normal to the plate plane. The linear intercept as measured above, should give a good description of the particle size along this diffusion direction.

4.9 Bulk extraction of carbides and X-ray diffraction

It is possible to isolate the carbide precipitates in steels by the electrochemical dissolution of the matrix. X-ray diffraction of the extracted particles can then be used for identification and quantitative analysis, including accurate lattice parameter measurements and volume fraction data for the various carbides formed in the steel during tempering. This technique is discussed in detail by Andrews and Hughes (1958), and more recently by Stuart and Ridley (1966), Leitnaker *et al.* (1975), Pilling and Ridley (1982) and Stevens and Lonsdale (1987).

In particular Stevens and Lonsdale (1987) investigated the experimental conditions necessary for optimum carbide extraction. The composition and strength of the electrolyte and the conditions of voltage or current density determine the efficiency with which dissolution of the matrix occurs whilst leaving the carbide precipitates intact. Chemical dissolution of the extracted precipitates in the electrolyte can occur. This is dependent on the electrolyte and the temperature and time of the extraction. The use of high voltages and associated high current densities results in large amounts of carbides being extracted in a short time; however, the likelihood of chemical dissolution of the precipitates may be increased by resistance heating of the electrolyte. The precipitates are more likely to separate from the specimen and fall into the solution thus increasing their risk of loss. The literature suggests that 5% aqueous hydrochloric acid is suitable for the extraction of low alloy steels, whereas 10% alcoholic hydrochloric acid is usually used for high alloy steels. The disadvantages of the alcohol as a base are that the lower associated current densities result in a higher acid concentration and longer extraction times having to be used, enhancing chemical dissolution of extracted carbides. Stevens and Lonsdale (1987) also suggest that for steels containing the carbide M_3C using alcohol as a base may mean that few of these carbides are extracted.

The specimen was anodically dissolved in a cell with a platinum cathode and a solution of 5% hydrochloric acid in water for the $2\frac{1}{4}Cr1Mo$ steel and 10% hydrochloric acid in methanol for the $12Cr1MoV$ steel as the electrolyte at a voltage of 1.5 V. Typical extraction times were 6–8 hours. The electrolyte was then decanted off and the precipitate thoroughly dried in an oven at approximately 60°C. Careful weighing at all stages of the extraction to an accuracy of 10 μg

was performed to find the exact amount of precipitate extracted. An internal standard, CeO_2 , was added to the precipitates. This was accurately weighed to approximately 25% of the total mass of the precipitate. A Siemens D500 diffractometer (CuK_α radiation) was used to scan between 30° and $65^\circ 2\theta$ at a step size of 1 second duration, corresponding to $0.004^\circ 2\theta$, where θ is the Bragg angle. The diffraction peak positions were located using Siemens DIFFRAC 500 software, also used to calculate the associated integrated intensities of the peaks.

CHAPTER 5

$2\frac{1}{4}$ Cr1Mo STEEL

Extensive studies of cementite composition changes in bainitic and mixed microstructures of bainite and allotriomorphic ferrite are discussed in this chapter. The observed composition changes are found to be highly dependent on the position of the carbides within the microstructure and on the particle size. The transformation of the cementite to alloy carbides is also studied. It is found that alloy carbides precipitate with a composition very close to their equilibrium composition and therefore subsequent enrichment is negligible.

CHAPTER 5

$2\frac{1}{4}$ Cr1Mo STEEL

5.1 Introduction

$2\frac{1}{4}$ Cr1Mo steel is widely used for superheater tubing in power plant, and as filler materials for joining $\frac{1}{2}$ Cr $\frac{1}{2}$ Mo $\frac{1}{4}$ V steam piping. Its creep properties, and their correlation with microstructural changes, have been studied widely (e.g. Baker and Nutting, 1959; Hale, 1975; Klueh, 1978). It is well established that the creep properties improve with subsequent tempering and then eventually degrade after the precipitation of the larger equilibrium alloy carbides. $2\frac{1}{4}$ Cr1Mo steel is usually given a stress-relief heat treatment at 700°C before going into service at a temperature of approximately 565°C. Klueh (1978) states that the creep rate is controlled initially by the motion of dislocations which contain atmospheres of carbon and possibly molybdenum clusters, and subsequently by atmosphere-free dislocations moving through M_2C precipitates.

The high temperature mechanical properties of the material are affected strongly by the metallurgical instability of the alloy involving carbide precipitation reactions. The tempering process results initially in the formation of iron carbides, which are subsequently replaced by more stable alloy carbides. Many studies of the precipitation sequences in $2\frac{1}{4}$ Cr1Mo steels have been made. Baker and Nutting (1959) discuss precipitation sequences in a commercial alloy in both quenched and normalised conditions in the temperature range 673–1023K. Andrews *et al.* (1972) have produced a comprehensive set of ‘near-equilibrium’ experimental diagrams relating to carbide stability. They used many steels in the composition ranges 0–6 wt.% Cr, 0–2 wt.% Mo and 0–1wt.% V, and tempered as-quenched microstructures for up to 1000 hours at 923 and 973K. Titchmarsh (1978) studied carbide precipitation in samples tempered at 933K for up to 200 hours in order to demonstrate the identification of various carbides using EDX analysis techniques. Hipsley (1981) also studied $2\frac{1}{4}$ Cr1Mo steel, although this was in the context of cracking during the stress-relief heat treatment in the bainitic Heat-Affected-Zone (HAZ) of welds. Pilling and Ridley (1982) investigated the effect of carbon content in three low carbon $2\frac{1}{4}$ Cr1Mo alloys, tempering at 700°C.

Baker and Nutting (1959) found that the sequences of carbide precipitation in the normalised (ferritic/bainitic) and quenched (autotempered martensite) microstructures were almost identical. The only difference being that precipitation of M_2C occurred in the early stages of tempering the normalised steel, and persisted in the ferrite phase, forming well-defined flat-

tened needles. They also found that bainitic carbides spheroidised quickly during tempering at 600°C. After 50 hours Cr_7C_3 was found in the bainite near the bainite/ferrite interface, M_{23}C_6 then being found in the bainitic regions, and only in the regions which were free from Cr_7C_3 . The experimental results of Baker and Nutting are presented in Figure 5.1.

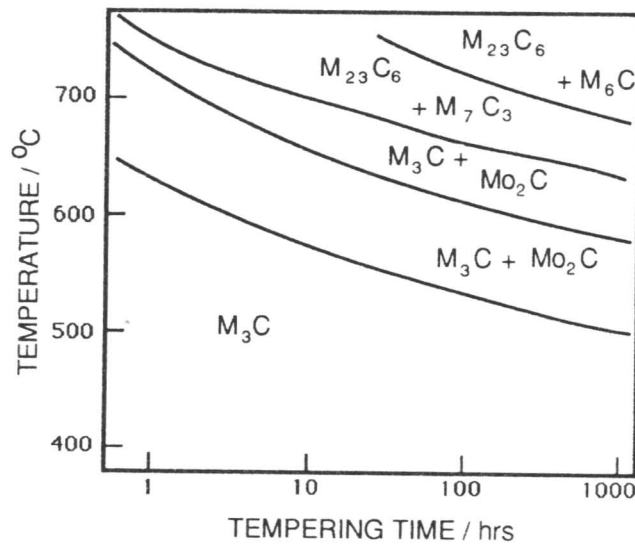


Figure 5.1: Carbide stability diagram for a $2\frac{1}{4}\text{Cr}1\text{Mo}$ steel. (Modified from Baker and Nutting, 1959)

There is evidence to suggest that small changes in chemical composition can alter the precipitation behaviour of the alloy. Yu (1989) has shown that increasing the silicon concentration stabilises M_6C , and accelerates the precipitation of M_2C . Similarly an increase in the manganese concentration was found to accelerate the precipitation of M_7C_3 . An analysis based on the thermodynamic stability as a function of chemistry and temperature could in principle be used to explain these results. However, no information can be obtained on the rate of precipitation from such calculations. In stating such precipitation sequences, it is important to relate them to the part of the microstructure in which they occur. Lee (1989) has recently confirmed that the starting microstructure can have a profound effect on the tempering sequence. In a Fe-1Cr-0.5Mo-0.15C wt.% steel detailed differences between pearlitic, bainitic and ferritic microstructures were demonstrated, and it was also shown that the carbide type was sensitive to position within the microstructure. The predicted equilibrium carbides in the steel utilised in this work using MTDATA were M_6C and M_{23}C_6 in the temperature range 500–650°C.

5.2 Materials

The $2\frac{1}{4}\text{Cr}1\text{Mo}$ steel was supplied in the form of a cylindrical bar approximately 100 mm in diameter and 300 mm long. Rectangular specimens of size 10×10×60 mm were machined from

the bar for furnace heat-treatment, and smaller cylindrical specimens of 8 mm diameter and 12 mm length were also machined for use in the thermomechanical simulator. The chemical composition of the steel (in wt. %) is given in Table 5.1.

Table 5.1: Chemical composition of $2\frac{1}{4}$ Cr1Mo steel in wt. %

C	Si	Mn	P	S	Cr	Mo	V	Ni	Cu	Al	Co	As	Sn
0.15	0.29	0.49	0.01	0.025	2.20	0.96	0.01	0.14	0.18	< 0.01	0.02	0.03	0.02

5.3 Initial heat treatments

The initial microstructure for use in power plant is formed by continuously cooling a thick section of material, resulting in a mixture of allotriomorphic ferrite and bainite (with some martensite). In this work it was decided to investigate both a predominantly bainitic microstructure (also containing some areas of martensite) and a mixed microstructure of approximately 50% allotriomorphic ferrite and bainite. [The former microstructure is henceforth referred to as ‘fully bainitic’ for brevity, although it should always be understood that it consists of a mixture of bainitic ferrite and martensite.] The bainite in the specimens containing 50% allotriomorphic ferrite forms from carbon-enriched austenite and therefore the enrichment kinetics of the cementite are expected to be different from those in the fully bainitic microstructure. In order to determine the heat treatments required to produce these two starting microstructures it is necessary to calculate the time-temperature-transformation (TTT) diagram for the steel.

5.3.1 Calculation of the TTT curve and phase diagram

A model developed by Bhadeshia (1982) was used to calculate the TTT curve and phase diagram for the $2\frac{1}{4}$ Cr1Mo steel; the results are presented in Figure 5.2 and Figure 5.3. (The ‘kinks’ in the dot-dashed line in Figure 5.2 and in the Ae_3' line in Figure 5.3 are artefacts of the computer program.) The phase diagram shows three distinct lines: the line T_0 is the locus of points where ferrite and austenite of identical composition have equal free energy and the T_0' line is a modification of this which allows for the strain energy involved in the transformation (400 J mol^{-1}). The line Ae_3' is the paraequilibrium phase boundary indicating equilibrium between ferrite and austenite when the ratio of iron to substitutional solute atoms is constant everywhere, i.e. when there is no substitutional alloying element partitioning during transformation. The start temperatures B_s and M_s for the bainite and martensite reactions respectively are also marked on the TTT curve. The TTT curve was then used to determine a suitable heat treatment cycle. To produce a mixed microstructure of allotriomorphic ferrite and bainite it can be seen

that holding the specimen at 700°C will allow the growth of allotriomorphic ferrite and further transformation at 480°C, within the bainite phase field, will produce bainite. A fully bainitic microstructure can be produced by simply holding the specimen at 480°C.

5.3.2 Calculations to determine the volume fraction of allotriomorphic ferrite

A model has been developed by Bhadeshia *et al.* (1987) to calculate the volume fraction of allotriomorphic ferrite formed in steel weld deposits. This theory was applied to the 2 $\frac{1}{4}$ Cr1Mo steel to estimate the volume fraction of allotriomorphic ferrite in a sample after a given time for transformation at 700°C. The calculation of the growth rate of allotriomorphic ferrite uses the methods discussed by Avrami (1939) and Cahn (1956) to calculate the isothermal reaction kinetics for ferrite allotriomorphs forming at grain boundaries, modified to incorporate parabolic growth kinetics. The allotriomorphs are modelled as discs parallel to grain boundary planes with a half-thickness, q . Geometrical considerations lead to the following approximate expression when the austenite boundary is decorated with uniform layers of allotriomorphic ferrite

$$-\ln(1 - \zeta) = \frac{2S_v}{\phi} \alpha_1 t^{\frac{1}{2}}, \quad (5.1)$$

where S_v is the austenite grain surface area per unit volume, α_1 is the one-dimensional parabolic thickening rate constant and t is the reaction time in seconds. ϕ is the equilibrium volume fraction of ferrite, given by

$$\phi = \frac{x^{\gamma\alpha} - \bar{x}}{x^{\gamma\alpha} - x^{\alpha\gamma}}, \quad (5.2)$$

where $x^{\gamma\alpha}$, $x^{\alpha\gamma}$ and \bar{x} are the carbon concentrations in the austenite, ferrite and the bulk alloy respectively. ζ is the calculated volume fraction of allotriomorphic ferrite divided by ϕ .

The values of $x^{\gamma\alpha}$, $x^{\alpha\gamma}$ and α_1 were determined using the same computer model as that for calculating the TTT curve. At 700°C these were 2.28 at.%, 0.0669 at% and 0.1014×10^{-3} cm s $^{-\frac{1}{2}}$ respectively. \bar{x} was 0.69 at.%. Assuming an initial austenite grain size of approximately 150 μ m, estimated from the prior austenite grain size in the bainitic specimens, gives a value of S_v equal to 13.33×10^3 m $^{-1}$. Therefore, for transformation at 700°C for 1 hour, theory predicts a volume fraction of allotriomorphic ferrite of $\simeq 0.6$. It can also be shown using the approximation $q = \alpha_1 t^{\frac{1}{2}}$, that a tempering time of 1 hour at 700°C is consistent with the above calculation. It was therefore decided that the transformation to allotriomorphic ferrite should be carried out initially for 1 hour at 700°C.

5.3.3 Starting bainitic microstructure

The rectangular specimens were first dip-coated in a commercial application (containing a dispersion of clays and refractory solids in a solution of an organic resin in solvent) whose